The Astrophysical Journal, 983:64 (20pp), 2025 April 10 https://doi.org/10.3847/1538-4357/adbd40

Polycyclic Aromatic Hydrocarbon and CO(2–1) Emission at 50–150 pc Scales in 70 Nearby Galaxies

Ryan Chown[1], Adam K. Leroy[1,2], Karin Sandstrom[3], Jérémy Chastenet[4], Jessica Sutter[3,5], Eric W. Koch[6], Hannah B. Koziol[3], Lukas Neumann[7,8], Jiayi Sun[9,36], Thomas G. Williams[10], Dalya Baron[11,12], Gagandeep S. Anand[13], Ashley. T. Barnes[8], Zein Bazzi[7], Francesco Belfiore[14], Frank Bigiel[7], Alberto Bolatto[15], Médéric Boquien[16], Yixian Cao[17], Mélanie Chevance[18,19], Dario Colombo[7], Daniel A. Dale[20], Jakob den Brok[6], Oleg V. Egorov[21], Cosima Eibensteiner[22,37], Eric Emsellem[8,23], Hamid Hassani[24], Jonathan D. Henshaw[25,26], Hao He[7], Jaeyeon Kim[12], Ralf S. Klessen[6,18,27,28], Kathryn Kreckel[21], Kirsten L. Larson[29], Janice C. Lee[13], Sharon E. Meidt[4], Eric J. Murphy[22], Elias K. Oakes[30], Eve C. Ostriker[9,31], Hsi-An Pan[32], Debosmita Pathak[1,2], Erik Rosolowsky[24], Sumit K. Sarbadhicary[1,2,33], Eva Schinnerer[26], Yu-Hsuan Teng[15], David A. Thilker[33], Tony D. Weinbeck[20], and Elizabeth J. Watkins[34]

[1] Department of Astronomy, The Ohio State University, 140 West 18th Avenue, Columbus, OH 43210, USA; rchown53@gmail.com
[2] Center for Cosmology and Astroparticle Physics (CCAPP), 191 West Woodruff Avenue, Columbus, OH 43210, USA
[3] Department of Astronomy & Astrophysics, University of California, San Diego, 9500 Gilman Drive, La Jolla, CA 92093, USA
[4] Sterrenkundig Observatorium, Universiteit Gent, Krijgslaan 281 S9, B-9000 Gent, Belgium
[5] Whitman College, 345 Boyer Avenue, Walla Walla, WA 99362, USA
[6] Center for Astrophysics | Harvard & Smithsonian, 60 Garden Street, Cambridge, MA 02138, USA
[7] Argelander-Institut für Astronomie, University of Bonn, Auf dem Hügel 71, 53121 Bonn, Germany
[8] European Southern Observatory (ESO), Karl-Schwarzschild-Straße 2, 85748 Garching, Germany
[9] Department of Astrophysical Sciences, Princeton University, Princeton, NJ 08544, USA
[10] Sub-department of Astrophysics, Department of Physics, University of Oxford, Keble Road, Oxford OX1 3RH, UK
[11] The Observatories of the Carnegie Institution for Science, 813 Santa Barbara Street, Pasadena, CA 91101, USA
[12] Kavli Institute for Particle Astrophysics & Cosmology (KIPAC), Stanford University, CA 94305, USA
[13] Space Telescope Science Institute, 3700 San Martin Drive, Baltimore, MD 21218, USA
[14] INAF—Osservatorio Astrofisico di Arcetri, Largo E. Fermi 5, I-50125, Florence, Italy
[15] Department of Astronomy and Joint Space-Science Institute, University of Maryland, College Park, MD 20742, USA
[16] Université Côte d'Azur, Observatoire de la Côte d'Azur, CNRS, Laboratoire Lagrange, 06000, Nice, France
[17] Max-Planck-Institut für Extraterrestrische Physik (MPE), Giessenbachstr. 1, D-85748 Garching, Germany
[18] Universität Heidelberg, Zentrum für Astronomie, Institut für Theoretische Astrophysik, Albert-Ueberle-Str 2, D-69120 Heidelberg, Germany
[19] Cosmic Origins Of Life (COOL) Research DAO[35]
[20] Department of Physics and Astronomy, University of Wyoming, Laramie, WY 82071, USA
[21] Astronomisches Rechen-Institut, Zentrum für Astronomie der Universität Heidelberg, Mönchhofstr. 12-14, D-69120 Heidelberg, Germany
[22] National Radio Astronomy Observatory, Charlottesville, VA, USA
[23] Univ Lyon, Univ Lyon 1, ENS de Lyon, CNRS, Centre de Recherche Astrophysique de Lyon UMR5574, F-69230 Saint-Genis-Laval, France
[24] Department of Physics, University of Alberta, 4-183 CCIS, Edmonton, AB T6G 2E1, Canada
[25] Astrophysics Research Institute, Liverpool John Moores University, 146 Brownlow Hill, Liverpool L3 5RF, UK
[26] Max-Planck-Institut für Astronomie, Königstuhl 17, D-69117, Heidelberg, Germany
[27] Universität Heidelberg, Interdisziplinäres Zentrum für Wissenschaftliches Rechnen, Im Neuenheimer Feld 205, 69120 Heidelberg, Germany
[28] Elizabeth S. and Richard M. Cashin Fellow at the Radcliffe Institute for Advanced Studies at Harvard University, 10 Garden Street, Cambridge, MA 02138, USA
[29] AURA for the European Space Agency (ESA), Space Telescope Science Institute, 3700 San Martin Drive, Baltimore, MD 21218, USA
[30] Department of Physics, University of Connecticut, 196A Auditorium Road, Storrs, CT 06269, USA
[31] Institute for Advanced Study, 1 Einstein Drive, Princeton, NJ 08540, USA
[32] Department of Physics, Tamkang University, No. 151, Yingzhuan Road, Tamsui District, New Taipei City 251301, Taiwan
[33] Department of Physics and Astronomy, The Johns Hopkins University, Baltimore, MD 21218, USA
[34] Jodrell Bank Centre for Astrophysics, Department of Physics and Astronomy, University of Manchester, Oxford Road, Manchester M13 9PL, UK
Received 2024 September 26; revised 2025 January 31; accepted 2025 February 17; published 2025 April 7

Abstract

Combining Atacama Large Millimeter/submillimeter Array CO(2–1) mapping and JWST near- and mid-infrared imaging, we characterize the relationship between CO(2–1) and polycyclic aromatic hydrocarbon (PAH) emission at ≈100 pc resolution in 70 nearby star-forming galaxies. Leveraging a new Cycle 2 JWST Treasury program targeting nearby galaxies, we expand the sample size by more than an order of magnitude compared to previous ≈100 pc resolution CO–PAH comparisons. In regions of galaxies where most of the gas is likely to be molecular, we find strong correlations between CO(2–1) and 3.3 μm, 7.7 μm, and 11.3 μm PAH emission, estimated from JWST's F335M, F770W, and F1130W filters. We derive power-law relations

[35] coolresearch.io
[36] NASA Hubble Fellow.
[37] Jansky Fellow of the National Radio Astronomy Observatory.

between CO(2–1) and PAH emission, with indices in the range 0.8–1.3, implying relatively weak variations in the observed CO-to-PAH ratios across our sample. We find that CO-to-PAH ratios and scaling relationships near H II regions are similar to those in diffuse sight lines. The main difference between the two types of regions is that sight lines near H II regions show higher intensities in all tracers. Galaxy centers show higher overall intensities and enhanced CO-to-PAH ratios compared to galaxy disks. Individual galaxies show 0.19 dex scatter in the normalization of CO at fixed $I_{\rm PAH}$, and this normalization anticorrelates with specific star formation rate and correlates with stellar mass. We provide a prescription that accounts for galaxy-to-galaxy variations, representing our best current empirical predictor to estimate CO(2–1) intensity from PAH emission, allowing one to take advantage of JWST's excellent sensitivity and resolution to trace cold gas.

Unified Astronomy Thesaurus concepts: Interstellar medium (847); Dust continuum emission (412); CO line emission (262); Disk galaxies (391); Dust nebulae (413); Extragalactic astronomy (506)

1. Introduction

Broad emission features at 3.3, 6.2, 7.7, 8.6, 11.2, and 12.7 μm, attributed to the stretching and bending modes of polycyclic aromatic hydrocarbons (PAHs; A. Leger & J. L. Puget 1984; L. J. Allamandola et al. 1989; J. L. Puget & A. Leger 1989; A. G. G. M. Tielens 2008), dominate the near- and mid-infrared (NIR and MIR) luminosities of star-forming galaxies (e.g., J. D. T. Smith et al. 2007; A. G. G. M. Tielens 2008; F. Galliano et al. 2018). Emission from PAHs has been used to trace the star formation rate (SFR; E. Peeters et al. 2004; D. Calzetti et al. 2007; F. Belfiore et al. 2023), interstellar radiation field, and PAH abundance (e.g., B. T. Draine et al. 2007; R. C. Kennicutt & N. J. Evans 2012; C. M. Whitcomb et al. 2023a; D. Baron et al. 2024b; J. Sutter et al. 2024). At large scales (from a few kiloparsecs to integrated galaxies), PAH emission also shows a close correspondence with CO emission, exhibiting strong correlations and nearly linear scaling relations between PAH and CO intensity over 3 orders of magnitude (see M. W. Regan et al. 2004; Y. Gao et al. 2019, 2022; R. Chown et al. 2021; A. K. Leroy et al. 2021, 2023a; C. M. Whitcomb et al. 2023a). This correlation resembles the one that has been observed for decades relating tracers of molecular gas and the overall dust content traced by extinction, millimeter-wave emission, and far-infrared emission (e.g., R. H. Hildebrand 1983; F. P. Israel 1997; A. K. Leroy et al. 2011; A. D. Bolatto et al. 2013; F. Galliano et al. 2018). CO emission traces the molecular gas in galaxies (e.g., A. D. Bolatto et al. 2013), and this has led to the suggestion that PAH emission may be used as a quantitative tracer of the interstellar medium (ISM), specifically molecular gas in star-forming galaxies. This prospect is particularly exciting because the widespread availability of maps tracing PAH emission from the Wide-field Infrared Survey Explorer (WISE), Spitzer, and now JWST means that high-resolution, high-sensitivity maps of the atomic and molecular ISM could potentially be produced from every image of PAH emission obtained using these telescopes. In principle, this could be done to higher redshifts than can be accessed with CO observations. Furthermore, the upcoming Spectro-Photometer for the History of the Universe, Epoch of Reionization and Ices Explorer satellite (O. Doré et al. 2018), which will provide full-sky spectral maps of PAH emission, could also in principle be used to make maps of the atomic and molecular ISM across all nearby galaxies.

Initial JWST imaging of nearby galaxies supports the idea that PAH emission may act as a cold, dense ISM tracer. JWST images using PAH-dominated filters resemble sharper, more sensitive versions of Atacama Large Millimeter/submillimeter Array (ALMA) CO maps for the same galaxies (A. K. Leroy et al. 2023b; K. M. Sandstrom et al. 2023b). These analyses showed an excellent quantitative correspondence between CO(2–1) and emission in the F770W and F1130W filters[38] at ≈100 pc scales (A. K. Leroy et al. 2023a), even suggesting that the PAH emission traces lower-density ISM emission into the H I-dominated parts of the ISM (K. M. Sandstrom et al. 2023b). However, these first studies focused on only four galaxies, and so the general relationship between CO and PAH emission at these 50–150 pc scales (similar to the sizes of molecular clouds, or "cloud scales") was not statistically robust. Fortunately, over its first two cycles of operations, JWST has nearly completed an extensive census of NIR and MIR PAH emission from 74 local ($D \lesssim 20$ Mpc) galaxies as part of the Physics at High Angular Resolution in Nearby Galaxies Survey (PHANGS) Cycle 1 and Cycle 2 Treasuries (see Appendix A). In addition to 0.″03–0.″8 (≈15–120 pc) resolution JWST images, all of these galaxies also have ≈1″ (≈50–150 pc) resolution CO(2–1) imaging from ALMA (A. K. Leroy et al. 2021).

In this paper, the first to take full advantage of the combined PHANGS-JWST Cycle 1 and 2 surveys, we use this large new set of ALMA and JWST data to make quantitative comparisons between CO(2–1) and PAH emission traced using JWST's F770W, F335M,[39] and F1130W filters. We consider the 70 nearby galaxies with current in-hand JWST and high-quality ALMA observations and address the following questions.

1. What are the median and scatter in the CO(2–1)/PAH band ratios across a representative sample of nearby star-forming galaxies at molecular cloud scales (50–150 pc)? What are the correlation strengths and best-fit parameters for the CO(2–1) versus PAH power-law scaling relationships?
2. Are there significant differences between the correlations measured for galaxy centers and galaxy disks or when contrasting emission near H II regions with diffuse emission? Such variations might be expected given the different distributions of MIR intensity from these regions (D. Pathak et al. 2024) and the observation of systematic suppression of PAH emission from inside H II regions (J. Pety et al. 2005; V. Lebouteiller et al. 2007; M. Compiègne et al. 2008; J. Chastenet et al. 2023a; O. V. Egorov et al. 2023; J. Sutter et al. 2024).
3. How does the observed CO(2–1)–PAH relationship vary from galaxy to galaxy? Does it change as a function of parameters that also correlate with dust and PAH

[38] The F770W filter is centered at 7.7 μm and is 1.95 μm wide. The F1130W filter is centered at 11.3 μm and is 0.73 μm wide.
[39] The F335M filter is centered at 3.362 μm and is 0.347 μm wide.

abundances or the interstellar radiation field? Or do these factors affect CO emission in a similar way to PAH emission, suppressing the impacts of environmental variations on the correlation?

We describe our expectations for this work in Section 2 and our approach in Section 3, present our results in Section 4, and discuss and summarize our conclusions in Sections 5 and 6. Throughout, we focus on F770W emission because it has the widest availability out of all of the PAH bands that we consider, in terms of the total number of galaxies observed and total area mapped.

2. Expectations

Throughout the analysis, we will reference the expectation for emission from stochastically heated PAHs subjected to a scaled version of the local interstellar radiation field and mixed with an ISM consisting of mostly molecular gas (e.g., B. T. Draine & A. Li 2007; M. Compiègne et al. 2010; B. T. Draine 2011). To first order, we expect

$$\begin{aligned} I_{\rm PAH} &\propto {\rm DGR} \times q_{\rm PAH} \times N_{\rm H_2} \times U \\ &\propto ({\rm DGR} \times q_{\rm PAH} \times X_{\rm CO} \times U) I_{\rm CO}, \end{aligned} \quad (1)$$

where $I_{\rm PAH}$ and $I_{\rm CO}$ are the observed intensities of PAH and CO emission, respectively; DGR is the dust-to-gas mass ratio; $q_{\rm PAH}$ is the PAH-to-dust mass fraction; U is the strength of the interstellar radiation field relative to that in the solar neighborhood ($q_{\rm PAH}$ and U are defined in B. T. Draine et al. 2007); and $X_{\rm CO}$ is the CO-to-H_2 conversion factor.

This equation indicates why we expect a scaling relation in the first place. It also indicates the factors that might lead to environmental variations in the $I_{\rm CO}/I_{\rm PAH}$ ratio and nonlinearities in the observed scaling relations, e.g., when $U \gtrsim 10^3$ (for more discussion, B. T. Draine & A. Li 2007; A. K. Leroy et al. 2023a, 2023b; K. M. Sandstrom et al. 2023b). For example, to first order, U is proportional to the local unextinguished $\Sigma_{\rm FUV} \propto \Sigma_{\rm SFR}$ (e.g., see recent simulations by N. B. Linzer et al. 2024), and so we expect PAH emission to be brighter where local star formation activity is more intense (though bear in mind the destruction of PAHs in H II regions mentioned above). We return to this expected correlation between $I_{\rm PAH}/I_{\rm CO}$ and star formation activity in Section 4.3. The hardness of the radiation field, variations in the dust-to-gas ratio, and PAH abundance variations may also be important, but in our selected molecular-gas-dominated regions of relatively massive galaxies, we mostly expect these to be second-order effects (see Section 4.3).

3. Data and Methods

We analyze 70 galaxies that have both high-resolution ALMA CO(2–1) imaging and JWST imaging tracing PAH emission. Our targets are all part of PHANGS (T. Williams et al. 2023), and as such they are relatively massive ($M_\star \gtrsim 10^{9.5}\,M_\odot$), star-forming (${\rm SFR}/M_\star \gtrsim 10^{-11}\,{\rm yr}^{-1}$), and moderate-inclination ($i \lesssim 70°$) galaxies within $D \lesssim 20$ Mpc (A. K. Leroy et al. 2021). The subset of 19 targets presented in J. C. Lee et al. (2023) and T. G. Williams et al. (2024) have both F1130W imaging and "nebular masks," which identify H II regions based on a morphological decomposition of the Hα emission observed by the Very Large Telescope's Multi-Unit Spectroscopic Explorer (VLT/MUSE; B. Groves et al. 2023). The remaining targets are part of a new Cycle 2 Treasury program, which we describe below and in Appendix A. These new targets lack F1130W imaging and are not systematically covered with optical integral field spectroscopy. They therefore lacking nebular masks. Both the JWST Cycle 1 and Cycle 2 data include the F335M filter, but the continuum subtraction needed to isolate the PAH emission has only reached a science-ready state for the Cycle 1 data (Section 3.1). Therefore, analyses that require nebular masks (Section 4.1) and/or F335M and/or F1130W are limited to our 19 Cycle 1 targets.

3.1. JWST Imaging of PAH Emission

We use JWST MIRI and NIRCam imaging of 19 galaxies from the PHANGS-JWST Cycle 1 Treasury (GO 2107, PI: J. Lee; J. C. Lee et al. 2023). These data cover the F335M, F770W, and F1130W bands, each of which captures a strong PAH feature (e.g., A. G. G. M. Tielens 2008). The F335M filter captures the prominent 3.3 μm feature, attributed to C–H stretching modes of small PAHs, while the F770W filter captures the 7.7 μm PAH feature, attributed to C–C stretching modes of larger PAHs, and the F1130W filter captures the 11.3 μm feature, attributed to C–H out-of-plane bending modes of larger PAHs (A. G. G. M. Tielens 2008).

We also analyze 51 galaxies from a new Cycle 2 Treasury (GO 3707; PI: A. Leroy), which we describe in Appendix A. These new observations include the F335M and F770W filters. From the 54 available Cycle 2 galaxies, we remove NGC 3344 due to the lack of CO(2–1) observations, NGC 5530 because the observations are still to be executed, and NGC 1068 because the background level in the JWST images remains too uncertain for the current analysis. In total, we analyze 70 galaxies. The distribution of gas-phase metallicities of these galaxies has a median $12 + \log {\rm O/H} = 8.49$ dex and robust standard deviation of 0.09 dex.

Reduction for both data sets was done using the PHANGS-JWST pipeline (`pjpipe`[40]), following T. G. Williams et al. (2024). `pjpipe` is a wrapper on `jwst`,[41] tailored to produce mosaics of images with extended emission.

The Rayleigh–Jeans tail of the stellar continuum contributes to F335M and F770W (more so for F335M). This contribution must be subtracted from the total surface brightnesses to obtain emission from PAHs. We calculate stellar-continuum-subtracted F770W surface brightness $I^{\rm PAH}_{\rm F770W}$ by subtracting F200W (Cycle 1) or F300M (Cycle 2) times a scaling factor (one factor per band) following J. Sutter et al. (2024). In our sample, the F770W stellar continuum correction ($\rm F770W_\star = 0.22 \times F300M$, or $0.13 \times$ F200W for Cycle 1) tends to be largest in the gas-poor, high stellar surface density inner regions of galaxies, including bars and bulges, which have high stellar-to-gas ratios. The coverage of F300M and F200W is smaller than that of F770W, so for pixels without F300M or F200W data, we subtract median($\rm F770W_\star/F770W$) $\times$ F770W, where the median (which is 2%–10%, in agreement with C. M. Whitcomb et al. 2023b) is computed separately for each galaxy.

For F335M data, the stellar continuum subtraction is critical to any estimate of PAH emission (K. M. Sandstrom et al. 2023a). We use the continuum-subtraction method defined by H. Koziol et al. (in preparation) based on K. M. Sandstrom et al. (2023a), where F300M and F360M (for Cycle 1) are

[40] https://pjpipe.readthedocs.io/en/latest/
[41] https://jwst-pipeline.readthedocs.io/en/latest/index.html

used to estimate the continuum. We denote the continuum-subtracted F335M surface brightness as $I_{\rm F335M}^{\rm PAH}$. A similar effort using F300M is underway for Cycle 2 but not yet ready, and so our analysis of $I_{\rm F335M}^{\rm PAH}$ focused only on the Cycle 1 targets.

The F770W filter also captures emission from hot, very small dust grains, but this has a small effect (in the 19 PHANGS-JWST Cycle 1 galaxies, 7.7 μm PAH emission is found to be about 5× brighter than the underlying continuum; D. Baron et al. 2024a), and we do not subtract any underlying dust continuum. In both data sets, we also masked out a few bright stars and background galaxies with elliptical apertures that cover all of the emission from these sources on top of the F770W images. We do not use any data within these apertures.

3.2. ALMA CO(2–1)

We use PHANGS–ALMA CO(2–1) observations, which are described in A. K. Leroy et al. (2021). All maps include short- and zero-spacing data and are expected to achieve full flux recovery. The native resolution is $\approx 1\farcs0$, varying slightly from galaxy to galaxy. We use a noisy but uniform and high-completeness version of the CO(2–1) maps to ensure that >90% of the CO flux enters our analysis and that our mean trends will be unbiased by signal-to-noise-based clipping of the CO data (see A. K. Leroy et al. 2023b). These "flat" maps are produced following L. Neumann et al. (2023) using a procedure analogous to spectral stacking (A. Schruba et al. 2011). For each line of sight, we integrate over a fixed-width velocity window around the local mean velocity defined via either low-resolution CO emission, Hα emission, H I emission, or a model of the circular rotation, according to whichever yielded the most complete coverage and coherent reference velocity field for each galaxy. The velocity window is adapted to the disk-average line width of each individual galaxy and can vary from 20 to 200 km s^{-1}. We additionally ensure that all significant CO emission is included by combining the fixed-width velocity mask with the "strict" mask from A. K. Leroy et al. (2021). These "flat" masks will capture all of the CO emission along each line of sight and have well-defined noise, making them ideal to calculate the mean CO(2–1) intensity, $I_{\rm CO}$, as a function of $I_{\rm PAH}$.

3.3. Environment Masks

We analyze how the CO-to-PAH correlations vary as functions of environment within galaxies, focusing on three specific environments: (1) galaxy centers; (2) regions outside galaxy centers with prominent nebular emission ("nebular regions"), which are $\gtrsim$80% H II regions but also include a ∼10% contribution from supernova remnants (J. Li et al. 2024); and (3) regions outside of centers and not covered by the nebular region mask ("diffuse regions"). Following D. Pathak et al. (2024), these three regions show distinct distributions of MIR intensity. These three regions likely show differences in radiation field strength and/or hardness, PAH abundance, H_2/H I ratio, and dust-to-gas ratio. Additionally, PAH emission is found to be systematically suppressed inside H II regions (J. Chastenet et al. 2023a; O. V. Egorov et al. 2023; R. Chown et al. 2024; J. Sutter et al. 2024).

We define galaxy centers using the masks in M. Querejeta et al. (2021), which are based on NIR stellar morphology, and nebular regions following F. Santoro et al. (2022) and B. Groves et al. (2023), which are based on ionized gas emission observed by the VLT/MUSE as part of the PHANGS-MUSE survey (E. Emsellem et al. 2022). The galaxy center masks are available for all targets, though only 53 of our targets have well-defined central regions. The rest of the targets do not have any pixels classified as being in a "center," and all of their pixels are included in the "disk" category. The nebular masks are available only for the 19 Cycle 1 targets, which restricts a subset of our analysis to that subsample. See D. Pathak et al. (2024) for further details on a similar application of these environment masks.

3.4. Analysis Approach

To quantify the observed relationship between CO and PAH emission, we compile all measurements of individual pixels for all 70 galaxies into a single table, with columns for each NIR and MIR band (Section 3.1), CO(2–1) intensity (Section 3.2), and the values of each mask (Section 3.3). To avoid introducing systematic uncertainties, we analyze CO(2–1) intensities and do not adopt a CO-to-H_2 conversion factor. In Appendix C, we describe how to use our results to estimate H_2 surface densities.

The CO(2–1) data have the coarsest angular resolution in this work. The CO resolution varies slightly from galaxy to galaxy. Over the range of distances of the galaxies in the sample, the working resolution for PHANGS–ALMA corresponds to a median of 98 pc with a 16%–84% range of 63–129 pc (Table 15 in A. K. Leroy et al. 2021). Using `webbpsf`[42]-generated JWST point-spread function (PSFs), we convolve all JWST PAH images to share the same resolution of the corresponding CO(2–1) data following G. Aniano et al. (2011) and T. G. Williams et al. (2024). Then we define an astrometric grid with pixels 1/3× the CO PSF FWHM in size so that approximately 9 pixels represent an independent measurement. We reproject the CO(2–1) intensity (in K km s^{-1}), JWST PAH intensity (in MJy sr^{-1}), and mask information onto this grid, noting whether the majority of the area in each pixel corresponds to a galaxy center, a nebular region, or neither. We correct all intensities to face-on values by scaling by $\cos i$, where i is the galaxy inclination from P. Lang et al. (2020) and/or A. K. Leroy et al. (2021). The sample consists of nearly face-on galaxies (median $\cos i = 0.7$), so this correction does not have a large impact on our analysis.

PAH emission is also expected to emerge from dust mixed with atomic gas (e.g., see K. M. Sandstrom et al. 2023b). To avoid lines of sight where H I is expected to make up most of the ISM, we consider only regions that have inclination-corrected $I_{\rm F770W}^{\rm PAH} \geqslant 0.5$ MJy sr^{-1} (see A. K. Leroy et al. 2023a for arguments about this specific value for "bright" emission). In Table 1, we report the percentages of flux or area that are classified as "bright" according to this criterion. Focusing on F770W-bright pixels means that we analyze the significant majority of flux in all bands across the sample. However, we do exclude a majority (48%) of the area in the maps outside galaxy centers and nebulae. Analysis of this faint, extended diffuse emission requires the inclusion of H I and will be the topic of future work.

The 3.3 μm PAH feature is >10× fainter than the 7.7 and 11.3 μm ones (e.g., J. Chastenet et al. 2023a; D. A. Dale et al. 2025), and the maps tend to be more limited by noise and systematic uncertainties related to continuum subtraction. As a

[42] https://webbpsf.readthedocs.io/en/latest/

Table 1
Fraction of Flux and Area Entering Analysis

Quantity	All (%)	Outside Centers (%)	Centers (%)	Nebular (%)	Diffuse (%)
F335M$_{\rm PAH}$[a]	100	100	100	100	100
F770W$_{\rm PAH}$[a]	94	93	100	99	89
F770W	93	91	100	99	86
F1130W	93	92	100	99	88
CO(2–1)	96	95	100	99	94
Area	51	51	90	82	47

Notes. Percentages of the flux or area in the full map captured in the subset of F770W-bright pixels with $I_{\rm F770W_{PAH}} \geqslant 0.5$ MJy sr^{-1} (see Section 3), by band and environment. Our analysis captures the majority of the flux in all bands but only includes about half the total observed area.
[a] F335M$_{\rm PAH}$ and F770W$_{\rm PAH}$ refer to intensity in those filters after stellar continuum subtraction. After this correction, both filters are expected to be dominated by PAH emission (Section 3.4).

result, we impose an additional threshold for analyzing the 3.3 μm emission, considering only lines of sight with $I^{\rm PAH}_{\rm F335M} > 0.1$ MJy sr^{-1}. This corresponds roughly to $I^{\rm PAH}_{\rm F770W} \gtrsim 2$ MJy sr^{-1} and was selected to catch the lines of sight where the 3.3 μm map yields robust detections at a resolution matched to ALMA. Our analysis of F335M images is limited to lines of sight with surface brightness above this threshold.

Using the matched-resolution measurements, we analyze the correlation between CO(2–1) emission and emission in PAH-dominated JWST filters. For each MIR band X, we record the Spearman rank correlation coefficient (r), as well as the median and scatter in the ratio $I_{\rm CO(2-1)}/I_X$. We then calculate a best-fit power law relating $I_{\rm CO(2-1)}$ to I_X. Because the PHANGS–ALMA CO maps are much less sensitive than the JWST F770W and F1130W maps at matched angular resolution (see A. K. Leroy et al. 2023b), we treat the MIR imaging as the independent (x) axis for this calculation. We construct logarithmically spaced bins in I^X_ν and then compute the median and scatter, captured by the 16%–84% range, of $I_{\rm CO(2-1)}$ within each bin.

We perform linear regression on these binned measurements[43] using `linmix`,[44] a hierarchical Bayesian method described in B. C. Kelly (2007). It performs a linear regression of y on x while incorporating measurement errors in both variables. We model the CO versus PAH emission relationship as

$$\log_{10} I_{\rm CO(2-1)} = m(\log_{10} I^X_\nu - x_0) + b, \quad (2)$$

where the pivot $x_0 \equiv$ median(x). Recentering the fit at x_0 ensures minimal covariance between the best-fit m and b.

4. Results

The top left panel of Figure 1 shows the correlation between CO(2–1) and star-subtracted F770W, $I^{\rm PAH}_{\rm F770W}$, for all F770W-bright pixels (Section 3.4) in all galaxies in our sample. Combining all 70 galaxies, we find a strong correlation between CO(2–1) and starlight-subtracted F770W emission at 50–150 pc resolution, with $r \approx 0.64$. Table 2 reports the best-fit relation derived from fitting the binned CO(2–1) as a function of $I^{\rm PAH}_{\rm F770W}$. Our measurements of the normalization $I_{\rm CO(2-1)}/I^{\rm PAH}_{\rm F770W} \approx 1.0$ K km s^{-1} (MJy sr^{-1})$^{-1}$ and the slope (Equation (2)) $m = 0.90 \pm 0.07$ agree reasonably well with previous work on much smaller samples or at lower resolution (R. Chown et al. 2021; A. K. Leroy et al. 2023a).

Our selection of bright pixels aims to include regions dominated by molecular gas. However, in the lowest $I^{\rm PAH}_{\rm F770W}$ bins (1 MJy sr^{-1} $\lesssim I^{\rm PAH}_{\rm F770W} \lesssim$ 30 MJy sr^{-1}), we do see evidence of a slightly steeper relation, indicating lower CO-to-PAH ratios. This likely indicates a contribution of PAH emission associated with atomic gas (or perhaps CO-dark H_2) in these bins. At $I^{\rm PAH}_{\rm F770W} \lesssim 0.1$ MJy sr^{-1}, we would expect this to become the dominant effect because H I-dominated regions feature little to no CO emission while PAHs may remain present and excited there (F. Boulanger & M. Perault 1988). In the aforementioned low-intensity regime of Figure 1, this would lead to a steeper, more scattered CO versus PAH relation and likely a stronger correlation between H I column density and $I^{\rm PAH}_{\rm F770W}$.

At higher $I^{\rm PAH}_{\rm F770W}$, the correspondence between CO and PAH emission appears stronger, with only modest $\approx\pm$0.2 dex scatter in the CO-to-PAH ratio in the high-intensity ($\approx$100 MJy sr^{-1}) bins. At lower $I^{\rm PAH}_{\rm F770W}$, which corresponds to most of the area, the scatter in CO at fixed $I^{\rm PAH}_{\rm F770W}$ appears somewhat higher, $\pm$0.5 dex. Much of this reflects the statistical noise in the PHANGS–ALMA CO maps, which often approaches $\approx\pm1$ K km s^{-1} in the "flat" CO maps that we use. Our averaging approach recovers the median trend well, but this leads to a large scatter in the data in faint regions of each galaxy. We note that the noise is normally distributed, which leads to asymmetric scatter when shown in log space.

4.1. Nebular and Diffuse Regions

A number of studies have already demonstrated suppression of PAH emission, likely due to PAH destruction, within H II regions (e.g., S. C. Madden et al. 2006; M. S. Povich et al. 2007; K. D. Gordon et al. 2008; J. Montillaud et al. 2013; J. Chastenet et al. 2023a; O. V. Egorov et al. 2023; A. Pedrini et al. 2024; J. Sutter et al. 2024), while the intense radiation fields around H II regions also lead them to stand out as the brightest features in MIR maps of galaxy disks (D. Pathak et al. 2024). We note that at the physical resolution of PHANGS/JWST, PAH emission is reduced but still detected inside H II regions.

The top right panel in Figure 1 separates sight lines in galaxy disks into those near H II regions and diffuse (i.e., all other) regions, and Table 2 presents our correlation analysis for these two regions separately. Perhaps surprisingly, we find median CO/F770W$_{\rm PAH}$ ratios in H II and diffuse regions to be quite similar, with H II regions exhibiting a ratio only $\approx$0.10 dex (1.25×) lower than diffuse regions (i.e., PAHs are slightly brighter relatively to CO near H II regions). The correlation strength near H II regions appears stronger than in diffuse regions ($r \approx 0.8$ versus $r \approx 0.5$), but this partially reflects that the sight lines near H II regions tend to be brighter and so less affected by the high statistical noise in the CO maps. The slightly steeper relationship observed for the diffuse regions reflects that diffuse sight lines with $I^{\rm PAH}_{\rm F770W} \gtrsim 10$ MJy sr^{-1} show slightly elevated CO/PAH ratios compared to nebular regions with similar intensities, which may be due to preferential destruction of CO compared to PAHs in nebular regions. This preferential destruction may be related to recent work

[43] Because of the large number of individual pixels, the mean CO(2–1) intensity is detected at high signal-to-noise in all bins.
[44] https://linmix.readthedocs.io/en/latest/index.html

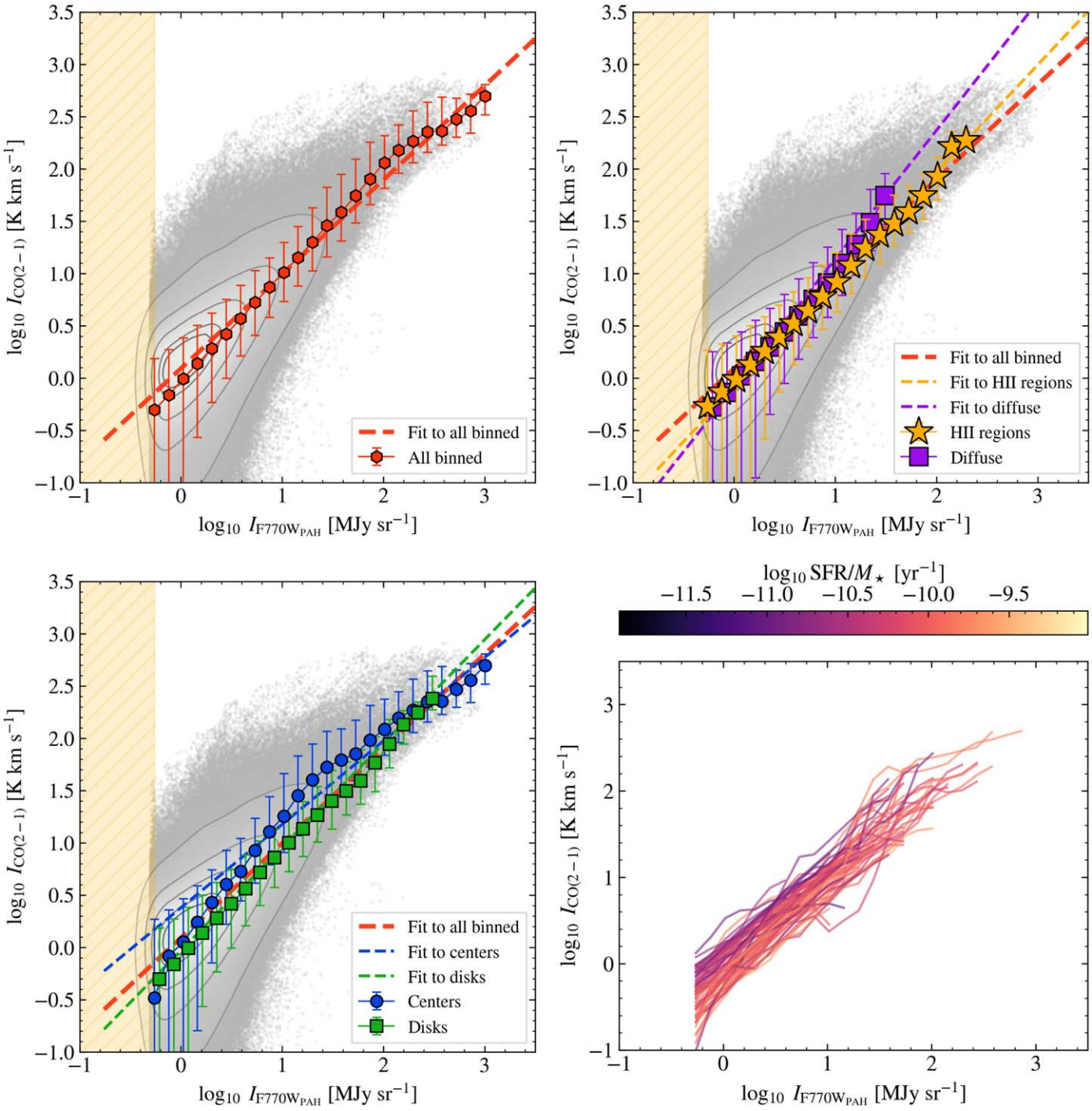

Figure 1. CO(2–1) and starlight continuum-subtracted F770W$_{\rm PAH}$ emission at ≈100 pc resolution in 70 nearby star-forming galaxies. Top left: all sight lines in our analysis (gray points) with data density contours enclosing the densest 15%, 25%, 50%, 75%, and 95% of the data points. The bins show the median and 16%–84% range of CO(2–1) emission in logarithmically spaced bins of $I_{\rm PAH}^{\rm F770W}$; treating the PAH emission as the independent variable allows us to average the noisier CO(2–1) data. The dashed line shows the best-fit power law describing these binned measurements (Table 2). Top right: same as the top left panel but now separately plotting results for sight lines near H II regions (yellow stars) and diffuse emission outside these regions (purple squares). The two environments show similar CO-to-PAH ratios where they overlap, but the sight lines near H II regions show overall brighter intensities. Bottom left: same as for the previous panels but now separating galaxy centers (blue circles) from disks (green squares). Galaxy centers show brighter emission and higher CO-to-PAH ratios at the same $I_{\rm F770W}^{\rm PAH}$. Bottom right: traces show binned results for each individual galaxy. The galaxies show overall similar CO(2–1) vs. F770W$_{\rm PAH}$ relations with moderate offsets from galaxy to galaxy. These offsets correlate with the integrated galaxy properties (see Figure 2, with the color bar indicating SFR/$M_\star$). See Table 2 for ratios and best fits for each panel.

demonstrating that PAH emission is slightly more long-lived than CO emission in gas-poor regions (J. Kim et al. 2025, in preparation). Sight lines with $I_{\rm F770W}^{\rm PAH} \lesssim 10\,{\rm MJy\,sr^{-1}}$ in Figure 1 show almost identical CO-to-PAH ratios for diffuse and nebular regions.

The similarity of the CO versus PAH relationship in diffuse and nebular regions likely results from the fact that the H II region masks that we use (from B. Groves et al. 2023) are based on data with coarse resolution (median 70 pc) compared to the actual size of most H II regions (e.g., see

Table 2
Ratios, Correlation, and Scaling Relations between PAH and CO(2–1) Emission

X	N_{gal}	N_{pix}[a]	$\log_{10}CO/X$	r	b	m	x_0	σ
All Pixels								
F335M$_{PAH}$	19	296,834	1.27 ± 0.38	0.58	1.38 ± 0.07	1.01 ± 0.10	0.10	0.44
F770W$_{PAH}$	70	2,090,731	0.03 ± 0.35	0.64	1.39 ± 0.06	0.90 ± 0.07	1.44	0.43
F770W	70	2,120,025	−0.00 ± 0.35	0.64	1.41 ± 0.07	0.91 ± 0.07	1.47	0.43
F1130W	20	972,892	−0.12 ± 0.37	0.63	1.20 ± 0.08	1.02 ± 0.09	1.34	0.44
All Pixels Outside of Centers								
F335M$_{PAH}$	19	279,910	1.25 ± 0.38	0.56	1.17 ± 0.07	1.04 ± 0.12	−0.05	0.44
F770W$_{PAH}$	70	2,041,245	0.02 ± 0.35	0.62	1.12 ± 0.07	0.98 ± 0.08	1.16	0.42
F770W	70	2,069,574	−0.01 ± 0.35	0.62	1.14 ± 0.07	0.99 ± 0.08	1.19	0.42
F1130W	20	946,437	−0.12 ± 0.37	0.62	0.93 ± 0.08	1.05 ± 0.13	1.11	0.44
All Pixels in Centers								
F335M$_{PAH}$	17	16,915	1.63 ± 0.34	0.80	1.65 ± 0.07	0.78 ± 0.09	0.10	0.41
F770W$_{PAH}$	58	49,469	0.18 ± 0.33	0.88	1.52 ± 0.07	0.80 ± 0.07	1.44	0.42
F770W	58	50,434	0.11 ± 0.34	0.87	1.51 ± 0.07	0.83 ± 0.07	1.47	0.44
F1130W	18	26,443	−0.02 ± 0.30	0.90	1.30 ± 0.07	0.97 ± 0.08	1.34	0.39
All Pixels in Nebular Regions (Cycle 1 Only)								
F335M$_{PAH}$	19	119,051	1.19 ± 0.33	0.70	1.13 ± 0.07	1.09 ± 0.12	−0.05	0.39
F770W$_{PAH}$	19	186,605	−0.02 ± 0.34	0.75	1.02 ± 0.09	1.03 ± 0.11	1.09	0.40
F770W	19	187,137	−0.04 ± 0.34	0.75	1.03 ± 0.08	1.06 ± 0.11	1.12	0.40
F1130W	19	194,681	−0.17 ± 0.33	0.76	0.89 ± 0.08	1.06 ± 0.12	1.11	0.40
All Pixels in Diffuse Regions (Cycle 1 Only)								
F335M$_{PAH}$	19	160,845	1.31 ± 0.40	0.44	0.95 ± 0.12	1.28 ± 0.32	−0.40	0.46
F770W$_{PAH}$	19	632,119	0.08 ± 0.38	0.52	0.72 ± 0.13	1.20 ± 0.27	0.66	0.47
F770W	19	642,906	0.05 ± 0.38	0.52	0.74 ± 0.13	1.21 ± 0.28	0.70	0.47
F1130W	19	727,342	−0.11 ± 0.38	0.54	0.68 ± 0.12	1.22 ± 0.25	0.81	0.47

Notes. Each section of the table reports results for a different data selection.
Columns: X—JWST band compared to CO(2–1), where the subscript "PAH" indicates that stellar continuum has been subtracted using overlapping NIRCam observations (Section 3.1); N_{gal}—number of galaxies entering this analysis; N_{pix}—number of sight lines entering the correlation analysis; $\log_{10}CO/X$—$\log_{10}$ of median ratio of CO(2–1) in K km s^{-1} to intensity in MJy sr^{-1} in band X with error indicating the scatter in the ratio estimated from the median absolute deviation; r—rank correlation between CO(2–1) and intensity in band X for all sight lines; b, m, x_0—best-fit power-law scaling parameters following Equation (2) relating CO(2–1) to intensity in band X; σ—rms scatter in dex of individual data about the best-fit scaling relation, inferred via the median absolute deviation.
[a] Pixels have size FWHM/3, so that there are 9 pixels per independent measurement.
[b] This scatter reflects the combined noise in the CO data, galaxy-to-galaxy scatter, and scatter about the fit within each galaxy. It is usually dominated by the noise in the CO data.

A. T. Barnes et al. 2022). As a result, these regions often include CO and PAH emission from ISM material projected toward but not actually inside H II regions. The CO and PAH emission may come from the well-shielded material surrounding the H II regions. J. Sutter et al. (2024) discuss a scenario in which the B. Groves et al. (2023) regions contain a mixture of diffuse material and true H II regions to explain observed F770W/F2100W ratios. Resolved comparisons of high ($\lesssim$10 pc) physical resolution Hα, Paα, CO, and MIR emission (e.g., A. Pedrini et al. 2024) should help test this hypothesis in the near future. Subtracting hot dust continuum emission from F770W, which we do not do, may also be important, since the filter still captures such emission in regions where PAHs have been destroyed to the point where their emission is not detectable.

4.2. Centers and Disks of Galaxies

Galaxy centers, especially bar-fed central molecular zones, differ from the disks of galaxies in ways that may also affect CO-to-PAH ratios. Galaxy centers exhibit some of the most intense star formation found in galaxies, with correspondingly high interstellar radiation fields and gas column and volume densities, and some host active galactic nuclei (e.g., E. Schinnerer et al. 2023; and see review in E. Schinnerer & A. K. Leroy 2024). As a result, CO in galaxy centers often exhibits broader line widths, lower opacity, and low X_{CO} (e.g., A. D. Bolatto et al. 2013; Y.-H. Teng et al. 2023).

The bottom left panel of Figure 1 shows the CO versus PAH relationship separating sight lines toward galaxy centers compared to those in disks. Both CO and PAH emission appear systematically brighter in galaxy centers than in disks, likely due to the higher densities and stronger radiation fields in galaxy centers. This is expected from previous analyses of these galaxies (e.g., J. Sun et al. 2020; D. Pathak et al. 2024). Sight lines in galaxy centers also appear offset toward higher CO intensity compared to disks at matched I^{PAH}_{F770W}. On average, the CO-to-PAH ratio is ≈0.16 dex (≈60%) higher in galaxy centers compared to disks, and the median $I_{CO(2-1)}$ in centers appears higher than that found for disks at fixed I^{PAH}_{F770W}.

We note one caveat here. The stellar continuum can also be bright in galaxy centers, and the starlight subtraction can become correspondingly more difficult (e.g., D. Baron et al. 2024b; J. Sutter et al. 2024). If our standard correction oversubtracts the starlight from F770W in galaxy centers, then we might artificially underestimate $F770W_{PAH}$. However, considering a similar situation, D. Baron et al. (2024b) found that the range of plausible starlight spectral energy distribution variations cannot impact the F770W emission enough to explain observed variations in the F770W/F1130W ratio in the inner parts of galaxies. We also note that we find a similar contrast between disks and centers in the CO-to-F1130W ratio, where F1130W is less affected by starlight. Finally, we note that we do not subtract any hot dust continuum from F770W. Hot dust continuum is likely stronger in galaxy centers, implying that our reported CO-to-PAH ratio measurements are lower than the true ratios.

A higher CO-to-PAH ratio in bright galactic centers may imply a large impact of X_{CO} on the measured ratio. A number of studies have shown that X_{CO} in galaxy centers can be 5–15 times lower than the standard Milky Way $X_{CO} = 2 \times 10^{20}\,cm^{-2}/(K\,km\,s^{-1})$ and $\approx 2\times$ lower than the galaxy mean on average (e.g., K. M. Sandstrom et al. 2013; F. P. Israel 2020; Y.-H. Teng et al. 2023; I.-D. Chiang et al. 2024). Following Equation (1), centrally suppressed X_{CO} will lead to centrally enhanced CO-to-PAH ratios. On the other hand, the intense radiation fields expected in galaxy centers should increase PAH emission and decrease the CO-to-PAH ratio, unless PAH destruction occurs. There is some evidence for slightly lower q_{PAH} in galaxy centers (J. Chastenet et al. 2023b), but a general trend is not so clear. Metallicity and DGR tend to be highest in galaxy centers, which may also decrease the CO-to-PAH ratio (see Equation (1)). Considering that most of these effects would decrease CO-to-PAH, the enhancement seen in Figure 1 and Table 2 may indicate that X_{CO} represents the dominant effect, offsetting these other PAH-enhancing effects.

4.3. Galaxy-to-galaxy Variations

So far, we have treated all galaxies together, separating sight lines into categories but not otherwise differentiating between targets. However, our sample spans a range of stellar mass ($M_\star$), SFR, metallicity, morphology, and more. These factors will influence U, DGR, q_{PAH}, and X_{CO}, so we might expect differences among the CO–PAH relationships for different galaxies (as in R. Chown et al. 2021). To explore the impact of these variations, the bottom right panel of Figure 1 shows that the CO-to-F770W relationship varies from galaxy to galaxy. The fits for individual galaxies are provided in Appendix B.

The bottom right panel of Figure 1 shows that individual galaxies exhibit strong CO–PAH correlations, mostly parallel to our best-fit overall relation. Broadly, the agreement among the 70 individual galaxies appears good, supporting the potential use of PAHs to trace CO. Specifically, the normalization of the CO–PAH relation scatters by ± 0.17 dex from galaxy to galaxy. Simply applying our best-fit overall relation to an individual galaxy with no additional information can be expected to yield a map biased by a factor drawn from this galaxy-to-galaxy scatter. This is similar to the pixel-by-pixel scatter observed within each galaxy, σ_{pix} in Table 4, implying that galaxy-to-galaxy variations and internal scatter contribute about equally to the total observed scatter.

In Figure 2, we test how these galaxy-to-galaxy offsets correlate with integrated galaxy properties. We compute the normalization of the best-fit CO(2–1) versus $F770W_{PAH}$ power law for each galaxy, C^{PAH}_{F770W}, by performing a linear fit of $\log_{10} I_{CO(2-1)}$ versus $\log_{10} I^{PAH}_{F770W}$ for each galaxy. C^{PAH}_{F770W} is then given by the value of the best-fit relation at $I^{PAH}_{F770W} = 1$ MJy sr^{-1}. We plot C^{PAH}_{F770W} against $M_\star$ and specific SFR (SFR/$M_\star$) (WISE+GALEX-based galaxy-integrated SFR and $M_\star$ are drawn from A. K. Leroy et al. 2021). Stellar mass correlates with the H_2/H I ratio, gas-phase metallicity, DGR, X_{CO}, and more (e.g., A. Saintonge & B. Catinella 2022). Meanwhile, SFR/$M_\star$ anticorrelates with q_{PAH} and correlates with the mean interstellar radiation field, $\bar{U}$ (J. Chastenet et al. 2025). Therefore, following Equation (1), both parameters might be expected to impact the CO-to-PAH ratio. Correlations between the galaxy-integrated CO-to-12 μm ratio (with the 12 μm data from WISE) with star formation activity, stellar mass, and SFR/$M_\star$ have previously been observed (R. Chown et al. 2021; A. K. Leroy et al. 2023a).

Consistent with previous work, we find a mild positive correlation between the CO/PAH ratio at fixed I^{PAH}_{F770W} and $M_\star$ and an anticorrelation between the CO/PAH normalization and SFR/$M_\star$. As seen in the bottom right panel of Figure 1, the galaxy-to-galaxy offsets are thus not random but agree with physical expectations. The $\log_{10} C^{PAH}_{F770W}$ versus $\log_{10}$SFR/$M_\star$ trend may indicate that the higher U associated with high-SFR/$M_\star$ galaxies leads to stronger PAH emission, offsetting any suppression due to lower q_{PAH} at high SFR/$M_\star$. As mentioned in Section 2, the anticorrelation between C^{PAH}_{F770W} and SFR/$M_\star$ is expected because the dust heating rate increases with SFR/$M_\star$. The $\log_{10} C^{PAH}_{F770W}$ versus $\log_{10} M_\star$ trend goes in the sense that galaxies with higher metallicity, DGR, and molecular-to-atomic gas ratios (e.g., A. Saintonge et al. 2017) show higher CO-to-PAH ratios. As a result, perhaps the low observed CO-to-PAH ratios seen in low-$M_\star$ systems reflect that the PAH emission is coming from regions dominated by H I or CO-dark H_2 despite our selection of only bright emission.

We also checked for correlations with distance and inclination to test how orientation and resolution might bias our results. We found that the normalization is uncorrelated with distance ($r = -0.04$, $p = 0.78$) and weakly correlated with $\cos i$ ($r = 0.24$, $p = 0.06$). Variations in $\cos i$ from galaxy to galaxy simply slide the data points parallel to a 1:1 relation. Since the best-fit slopes of CO(2–1) versus PAH emission for each galaxy and for the sample as a whole are within a few percent of 1.0, and furthermore, the sample covers a range of inclinations across the full $M_\star$ range, it is understandable that $\cos i$ does not have a significant effect.

We fit functional forms to the two trends and note the SFR/$M_\star$ as the stronger, clearer trend. These predict the normalization of the CO versus PAH relation as functions of galaxy-integrated $M_\star$ or SFR/$M_\star$:

$$\log_{10} C^{PAH}_{F770W} = 0.15 \pm 0.04 \quad (\log_{10} M_\star - 10.34) + 0.06 \pm 0.02, \tag{3}$$

$$\log_{10} C^{PAH}_{F770W} = -0.21 \pm 0.04 \quad (\log_{10} \mathrm{SFR}/M_\star + 10.14) + 0.03 \pm 0.02. \tag{4}$$

We provide best-fit parameters for normalizations versus $\log_{10} M_\star$ and $\log_{10}$SFR/$M_\star$ for the other PAH bands in Table 5.

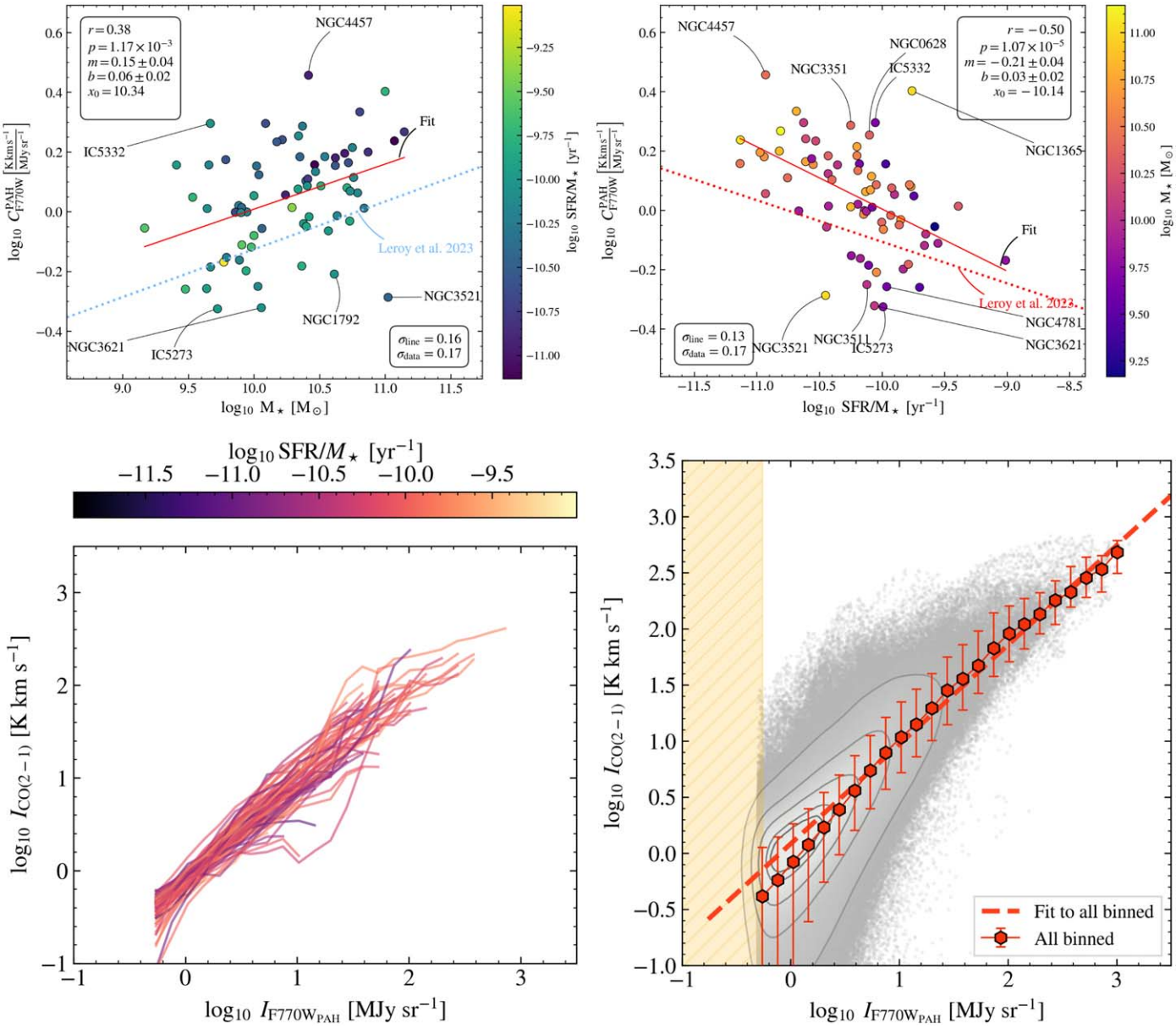

Figure 2. Galaxy-to-galaxy variations in the CO(2–1) vs. F770W$_{\rm PAH}$ relationship. CO(2–1) at fixed PAH intensity for individual galaxies (see bottom left panel of Figure 1) as a function of (left) galaxy-integrated stellar mass, $M_\star$, and (right) specific SFR, SFR/$M_\star$. Spearman's r; the p-value; the best-fit slope, intercept, and pivot ($y = m(x - x_0) + b$) to all galaxies; the scatter about the best-fit relation $\sigma_{\rm line}$ (Equation (3)); and the vertical scatter in the normalization $\sigma_{\rm data}$ are all indicated. Scaled versions of the best-fit normalizations of $I_{\rm CO(2-1)}$ vs. WISE 12 μm against stellar mass and SFR/$M_\star$ from A. K. Leroy et al. (2023a) are shown (dotted lines), showing similar trends. Galaxies further than 1.5$\sigma_{\rm line}$ from the best-fit lines are labeled. We observe a modest correlation between the CO-to-PAH ratio and $M_\star$ and a well-defined anticorrelation between the CO-to-PAH ratio and SFR/$M_\star$. The correlation with $M_\star$ may reflect increased contribution of PAH emission associated with CO-dark gas or atomic gas in low-mass galaxies. The anticorrelation with SFR/$M_\star$ likely reflects a mixture of increased radiation field strength, lower $X_{\rm CO}$, and enhancement of R_{21} in high-SFR/$M_\star$ galaxies, which appear to represent stronger effects than any $q_{\rm PAH}$. The bottom left panel shows the CO vs. F770W$_{\rm PAH}$ relationships for each galaxy normalized by $C^{\rm PAH}_{\rm F770W}$ predicted based on its $\log_{10}$SFR/$M_\star$. This normalization reduces the vertical scatter. The bottom right panel shows the fit to all pixels and all galaxies with the normalizations applied. We provide fit parameters for F770W$_{\rm PAH}$ in Equation (5) and for the rest of the bands in Table 5.

In the bottom panels of Figure 2, we normalize the data from each galaxy by the values predicted by this fit, aiming to remove galaxy-to-galaxy scatter. Then we refit the relation to all data (bottom right panel) and find

$$\log_{10} I_{\rm CO(2-1)} = (0.88 \pm 0.06)(x - 1.44) + (1.36 \pm 0.06), \quad (5)$$

with scatter $\sigma = 0.43$ dex, where $x \equiv \log_{10} I^{\rm PAH}_{\rm F770W} - \log_{10} C^{\rm PAH}_{\rm F770W}$ is shown in Table 6 along with prescriptions for the other two PAH bands. We describe how to use these prescriptions in Appendix C.

4.4. CO(2–1) and PAH Emission for Other Bands

So far we have focused only on the correlation between CO(2–1) and F770W$_{\rm PAH}$. Do the other PAH-tracing filters show similar correlations? In Figure 3, we show CO versus F335M$_{\rm PAH}$ and versus F1130W for our 19 Cycle 1 targets. The median CO/PAH ratios, fits, and statistics for these bands are shown in Table 2. The correlation remains strong in both of these bands, and the best-fit binned CO–PAH slopes are also very close to linear for the 3.3 μm and 11.3 μm features. Of the three PAH bands, F335M$_{\rm PAH}$ is the faintest (J. Chastenet et al. 2023b;

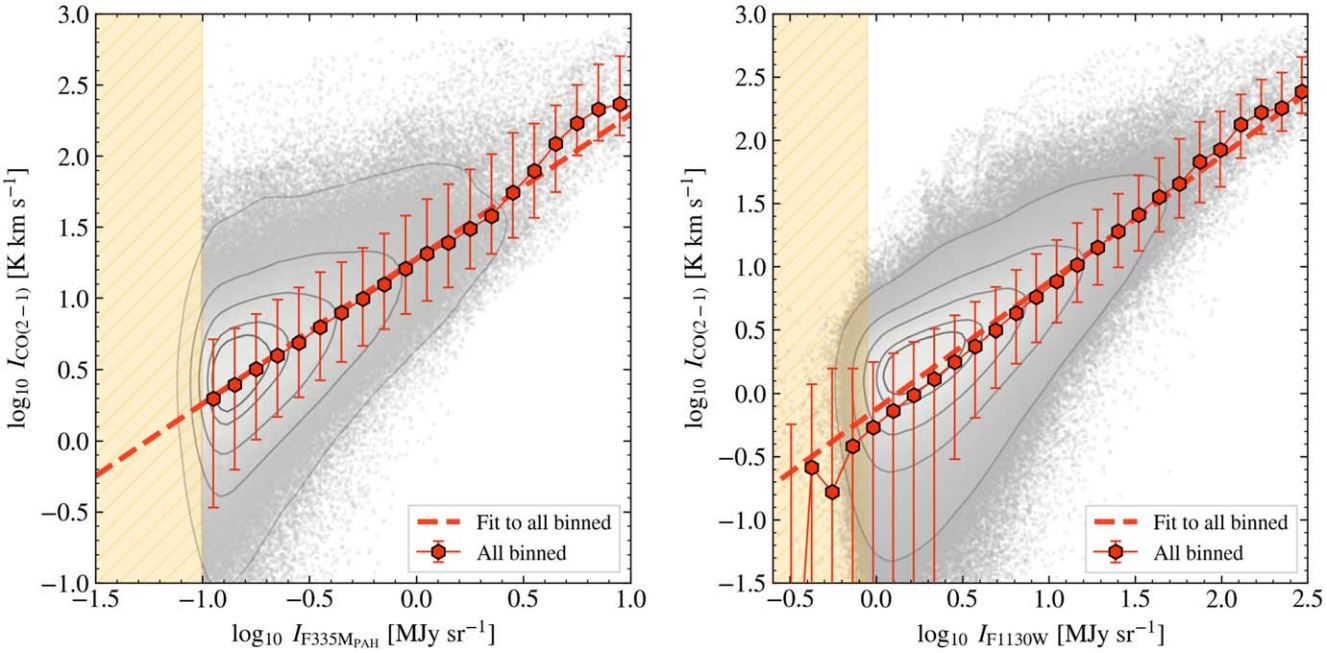

Figure 3. CO(2–1) intensity as functions of 3.3 μm and 11.3 μm PAH intensity. Same as Figure 1 but now showing PAH intensity captured by (left) the F335M filter capturing the 3.3 μm PAH feature (after continuum subtraction following H. Koziol et al. 2025, in preparation) and (right) the F1130W filter capturing the 11.3 μm PAH feature. The relationship between CO(2–1) and these bands resembles that which we observe for F770W$_{PAH}$ in Figure 1, though the specifics of the fits differ (Table 2). Of note, the F335M$_{PAH}$ feature has a lower intensity than the others, and extracting it from imaging depends critically on stellar continuum subtraction, but the shorter wavelength means that the band offers even higher resolution compared to the other features (see K. M. Sandstrom et al. 2023a).

K. M. Sandstrom et al. 2023a) and therefore shows the largest CO-to-PAH ratios ($10^{1.24} \approx 17.4$ times higher at F335M$_{PAH}$ than F770W$_{PAH}$, while F1130W is a factor of $10^{0.15} \approx 1.4$ times lower than F770W$_{PAH}$); see top rows of Table 2.

These three PAH bands (3.3, 7.7, and 11.3 μm) are dominated by different species of the PAH population—smaller, neutral PAHs for 3.3 μm; ionized PAHs for a range of sizes for 7.7 μm; and larger, mainly neutral PAHs for 11.3 μm. Their intensity ratios also respond to changes in the interstellar radiation field spectrum (e.g., A. Maragkoudakis et al. 2020; B. T. Draine et al. 2021). All three bands yield reasonable first-order estimators of CO intensity, but we would not expect all three to show identical or even equally good correlations with CO. We anticipate that future work will explore optimal combinations of bands to trace CO (and H_2) and examine the impact of conditions in the molecular gas on PAH band ratios.

From a practical perspective, each band has advantages. The F770W band traces the brightest PAH feature and is available now for >70 nearby galaxies. The F335M filter offers even sharper resolution but harbors the fainter 3.4 μm PAH feature, the Pfund-δ line (e.g., E. Peeters et al. 2024), and is more strongly affected by contamination by starlight. Meanwhile, the F1130W filter is largely unaffected by starlight and also captures a bright feature in a relatively narrow filter.

5. Discussion

We show that PAH emission can be used to predict CO(2–1) emission with ≈0.5 dex (i.e., a factor of ≈3) scatter at 100 pc resolution in the disks of star-forming galaxies without requiring any other information. Doing so, one expects an ≈±0.2 dex bias in any given prediction due to galaxy-to-galaxy variations in the CO-to-PAH ratio, which correlates with both $\log_{10}\mathrm{SFR}/M_\star$ and $\log_{10} M_\star$. We provide prescriptions to account for these galaxy-to-galaxy variations, which can sharpen the prediction even more. Figure 4 shows an example of such a prediction for the nearby spiral NGC 2903.

Our results formally apply to regions where molecular gas is likely to constitute a significant fraction of the ISM, with $\Sigma_{\mathrm{mol}} \gtrsim 4\,M_\odot\,\mathrm{pc}^{-2}$. It is likely that in fainter regions, the PAH emission reflects the distribution of atomic gas (see K. M. Sandstrom et al. 2023b), but the details of that correlation remain less well constrained, including the dependence of PAH abundance on H I phase and density (B. S. Hensley et al. 2022). We also emphasize that our results offer a way to predict CO emission, specifically CO(2–1) emission for regions with $I^{\mathrm{PAH}}_{\mathrm{F770W}} > 0.5$ MJy sr^{-1}. The CO(2–1)-to-H_2 conversion factor is known to vary as a function of environment across galaxies, and this will need to be included to predict the gas column density, $N(H_2)$ (e.g., see reviews in A. D. Bolatto et al. 2013; E. Schinnerer & A. K. Leroy 2024).

Despite these limitations, the CO–PAH correlation represents a powerful tool. In a matter of minutes on the source, JWST can produce maps with resolution and gas column sensitivity that would take ALMA many hours to match (of course ALMA carries kinematic information and CO represents a well-calibrated gas tracer, so the two remain complementary). As an example of the applications of such data, D. Pathak et al. (2024) analyzed 19 of the same galaxies we study to infer column density probability distribution functions at high physical resolution, suitable for benchmarking simulations and inferring some aspects of interstellar turbulence and galactic dynamics (S. E. Meidt et al. 2023; D. A. Thilker et al. 2023).

While the practical applications of the observed correlation are exciting, the stability of the CO-to-PAH ratio across a wide range of systems may reflect that the terms in Equation (1) have counterbalancing environmental dependencies. The interstellar

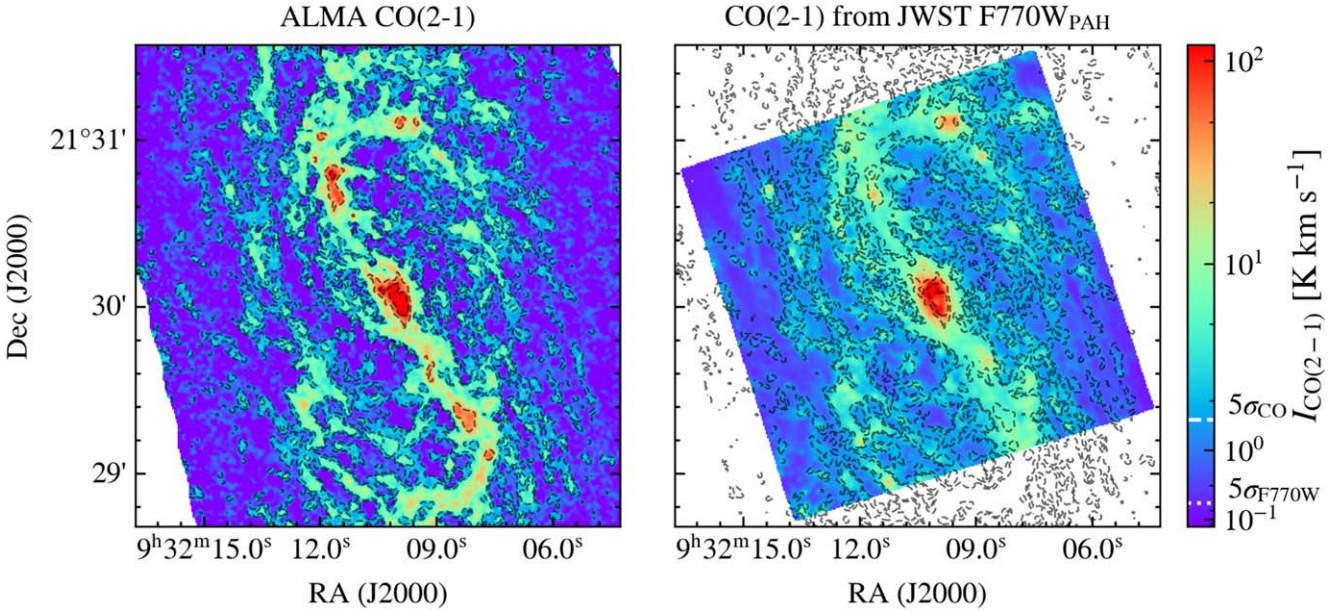

Figure 4. Predicting CO from PAH emission in one nearby galaxy. The left panel shows an inclination-corrected ALMA CO(2–1) image of NGC 2903 with contours at 1.25, 3.1, 31, and 100 K km s^{-1}. The right panel shows a predicted CO(2–1) intensity map based on JWST F770W$_{PAH}$ and the prescription in Equation (5). The F770W$_{PAH}$ image is masked to the NIRCam footprint as required for starlight subtraction (Section 3.1). The contours, which are the same in both panels, show a very close correspondence between CO and PAH emission. At the same time, CO(2–1) emission is underestimated in the bar ends, highlighting improvements to be explored in future work. This figure also shows the improved sensitivity of JWST compared to ALMA at recovering faint emission, with the 5σ rms noise indicated on the color bar.

radiation field varies within and among galaxies (e.g., B. T. Draine et al. 2007; G. Aniano et al. 2020; J. Chastenet et al. 2025), as does X_{CO}, and q_{PAH} appears strongly suppressed within H II regions (J. Chastenet et al. 2023a; O. V. Egorov et al. 2023; J. Sutter et al. 2024). This might reflect that environmental effects are somewhat offset, e.g., because U is higher where R_{PAH} (O. V. Egorov et al. 2023), as well as that q_{PAH} and α_{CO} tend to be low. Alternatively, they might reflect that the emitting PAHs tend to reside predominantly in neutral, moderately shielded gas, subjecting them to some of the same selection effects that apply to CO.

Beyond speculation, having established the basic observational correlations, the clear next step in this area is to follow up with a physically oriented analysis. The full PHANGS data sets make it possible to combine 21 cm data on atomic gas and best-estimate α_{CO} with estimates of the local interstellar radiation field, U, and PAH abundance, q_{PAH}, to test the physical expectation that $I_{PAH}/N(H) \propto U q_{PAH}^{-1}$. This will both illuminate the reasons for the tightness of the PAH–CO correlation and sharpen the use of PAH emission as an ISM tracer, particularly in the atomic-gas-dominated parts of galaxies.

6. Conclusions

We characterize the relationship between CO(2–1) and NIR and MIR PAH emission at ≈100 pc scales for 70 nearby ($D \lesssim 20$ Mpc) star-forming galaxies observed as part of PHANGS–ALMA and the PHANGS-JWST Cycle 1 and Cycle 2 Treasuries. This is by far the largest comparison of molecular gas tracers and PAH emission at cloud scales to date, more than 10× larger than initial JWST studies. We find the following.

1. CO(2–1) exhibits strong correlations with the PAH emission captured by JWST's F770W, F335M, and F1130W filters. In regions of galaxies where molecular gas is likely to make up most of the ISM ($I_{F770W} > 0.5$ MJy sr^{-1}; $\Sigma_{mol} \gtrsim 4\,M_\odot$ pc^{-2}), this correlation appears approximately linear ($0.8 \lesssim m \lesssim 1.2$) and covers more than 2 orders of magnitude in PAH and CO intensities. We provide power-law scaling relations that can be used to predict CO(2–1) from PAH emission (Table 2, Figure 1). The typical sight-line-to-sight-line scatter about these relations considering the whole sample together is $\sigma \approx 0.5$ dex and dominated by statistical noise in the CO measurements in our data set.
2. Subdividing the 19 JWST Cycle 1 targets into sight lines near H II regions and diffuse sight lines, we find overall similar scaling relationships between CO(2–1) and I_{F770}^{PAH} between the two types of regions (Table 2, Figure 1). The main difference appears to be that the nebular regions harbor more high-intensity sight lines than the diffuse regions (see also D. Pathak et al. 2024). This is consistent with the idea that the nebular regions still contain some well-shielded, denser gas outside the actual H II regions that harbor both CO and PAH molecules (see also J. Sutter et al. 2024).
3. We also contrast galaxy centers with emission from the surrounding disks, finding that galaxy centers exhibit on average an ≈0.2 dex (≈60%) higher ratio of CO(2–1)-to-F770W emission compared to galaxy disks (in addition to being brighter in both tracers, as in D. Pathak et al. 2024). This might reflect that the enhanced CO emission (i.e., low α_{CO}) in galaxy centers (e.g., Y.-H. Teng et al. 2023; I.-D. Chiang et al. 2024) represents a stronger effect than any enhancement in PAH emission due to a more intense interstellar radiation field. Because of this contrast, when fitting emission from both disk and central regions, the slope of the CO versus PAH relation tends to be somewhat steeper than what we observe for disks or centers alone.

4. Individual galaxies show similar relations between CO(2–1) and PAH intensity but with $\approx\pm0.2$ dex scatter in the normalization. The ratio of CO at fixed PAH intensity for a galaxy correlates with its stellar mass, $M_\star$, and anticorrelates with its specific SFR, SFR$/M_\star$, in good agreement with results for integrated galaxies using WISE. We provide prescriptions to predict resolved CO emission from PAH emission that also take into account galaxy-dependent normalizations, and these represent our best overall predictor.
5. We also present scaling relations and observe strong correlations linking CO(2–1) and emission in the PAH-dominated F1130W filter as well as continuum-subtracted F335M$_{\rm PAH}$ emission. The F1130W band has coarser resolution but is least affected by starlight contamination out of the three PAH-tracing bands we consider. The fainter F335M$_{\rm PAH}$ emission offers the prospect of tracing CO at the highest resolution but depends sensitively on stellar continuum subtraction (K. M. Sandstrom et al. 2023a; A. D. Bolatto et al. 2024; H. Koziol et al. 2025, in preparation).

Acknowledgments

This work has been carried out as part of the PHANGS collaboration. This work is based on observations made with the NASA/ESA/CSA JWST. The data were obtained from the Mikulski Archive for Space Telescopes at the Space Telescope Science Institute, which is operated by the Association of Universities for Research in Astronomy, Inc., under NASA contract NAS 5-03127 for JWST. These observations are associated with programs 2107 and 3707.

A.K.L., D.P., S.S., and R.C. gratefully acknowledge support from NSF AST AWD 2205628, JWST-GO-02107.009-A, and JWST-GO-03707.001-A. D.P. is supported by the NSF GRFP. A.K.L. also gratefully acknowledges support by a Humboldt Research Award.

K.S., H.K., and J.S. acknowledge funding support from grants JWST-GO-02107.006-A and JWST-GO-03707.005-A. J.C. acknowledges funding from the Belgian Science Policy Office (BELSPO) through the PRODEX project "JWST/MIRI Science exploitation" (C4000142239). O.E. acknowledges funding from the Deutsche Forschungsgemeinschaft (DFG, German Research Foundation)—project ID 541068876.

J.K. is supported by a Kavli Fellowship at the Kavli Institute for Particle Astrophysics and Cosmology (KIPAC).

M.B. acknowledges support from FONDECYT regular grant 1211000 and by the ANID BASAL project FB210003. This work was supported by the French government through the France 2030 investment plan managed by the National Research Agency (ANR) as part of the Initiative of Excellence of Université Côte d'Azur under reference number ANR-15-IDEX-01.

D.C. and Z.B. acknowledge support by the Deutsche Forschungsgemeinschaft, DFG project number SFB1601-B3.

K.K. gratefully acknowledges funding from the Deutsche Forschungsgemeinschaft (DFG, German Research Foundation) in the form of an Emmy Noether Research Group (grant No. KR4598/2-1; PI: Kreckel) and the European Research Council's starting grant ERC StG-101077573 ("ISM-METALS").

R.S.K. acknowledges financial support from ERC via Synergy Grant "ECOGAL" (project ID 855130), from the German Excellence Strategy via the "STRUCTURES" Cluster of Excellence (EXC 2181—390900948), and from the German Ministry for Economic Affairs and Climate Action in project "MAINN" (funding ID 50OO2206). R.S.K. also thanks the 2024/25 Class of Radcliffe Fellows for their company and for highly stimulating discussions.

E.R. and H.H. acknowledge support from the Canadian Space Agency, funding reference 23JWGO2A07.

This paper makes use of the following ALMA data, which have been processed as part of the PHANGS–ALMA survey: ADS/JAO.ALMA#2012.1.00650.S, ADS/JAO.ALMA#2013.1.00803.S, ADS/JAO.ALMA#2013.1.01161.S, ADS/JAO.ALMA#2015.1.00121.S, ADS/JAO.ALMA#2015.1.00782.S, ADS/JAO.ALMA#2015.1.00925.S, ADS/JAO.ALMA#2015.1.00956.S, ADS/JAO.ALMA#2016.1.00386.S, ADS/JAO.ALMA#2017.1.00392.S, ADS/JAO.ALMA#2017.1.00766.S, ADS/JAO.ALMA#2017.1.00886.L, ADS/JAO.ALMA#2018.1.01321.S, ADS/JAO.ALMA#2018.1.01651.S, ADS/JAO.ALMA#2018.A.00062.S, ADS/JAO.ALMA#2019.1.01235.S, ADS/JAO.ALMA#2019.2.00129.S, ALMA is a partnership of ESO (representing its member states), NSF (USA), and NINS (Japan), together with NRC (Canada), NSC and ASIAA (Taiwan), and KASI (Republic of Korea), in cooperation with the Republic of Chile. The Joint ALMA Observatory is operated by ESO, AUI/NRAO, and NAOJ. The National Radio Astronomy Observatory is a facility of the National Science Foundation operated under cooperative agreement by Associated Universities, Inc.

Finally, we thank the anonymous referee for the helpful suggestions, which improved the quality of this paper.

Facilities: JWST, ALMA, VLT:Yepun.

Software: astropy (Astropy Collaboration et al. 2013, 2018, 2022).

Appendix A
Cycle 2 JWST Imaging of PHANGS Galaxies

During its Cycle 2 campaign, JWST observed 55 nearby galaxies as part of Treasury program GO 3707 "A JWST Census of the Local Galaxy Population: Anchoring the Physics of the Matter Cycle" (PI: Leroy; co-PIs: Kreckel, Lee, Rosolowsky, Sandstrom, Schinnerer). The targets were chosen to overlap the PHANGS–ALMA CO(2–1) survey (A. K. Leroy et al. 2021), accounting for some updated knowledge about the target selection. PHANGS–ALMA serves as the parent sample for surveys with the Hubble Space Telescope, AstroSat, MeerKAT, VLT-MUSE, and more (E. Emsellem et al. 2022; J. C. Lee et al. 2022; H. Hassani et al. 2023; C. Eibensteiner et al. 2024). Therefore, these observations immediately overlap a rich multiwavelength database that enables a wide variety of science related to PAHs, ISM structure, stellar feedback, star formation, and more.

Table 3 lists the targets of both the Cycle 1 and Cycle 2 PHANGS Treasury, along with the list of bands observed and the stellar mass and SFR for each target (mostly from A. K. Leroy et al. 2019, 2021). Figure 5 shows both samples in SFR–$M_\star$ parameter space. As of this writing, all but two of the Cycle 2 galaxies (NGC 5248 and NGC 5530) have been fully observed. Those two require partial repeated observations. The observations for NGC 5248 and NGC 5530 are expected to be completed by 2025 mid-July and 2025 late June, respectively.

The Cycle 2 survey complements the one described in J. C. Lee et al. (2023) and T. G. Williams et al. (2024). This

Table 3
PHANGS-JWST Galaxy Sample and Observations

Galaxy	$\log M_*$ ($M_\odot$)	$\log \mathrm{SFR}/M_*$ (yr^{-1})	Cycle	F150W	F187N	F200W	F300M	F335M	F360M	F770W	F1000W	F1130W	F2100W
IC 1954	9.67	−10.11	2	✓	✓	…	✓	✓	…	✓	…	…	✓
IC 5273	9.72	−9.99	2	✓	✓	…	✓	✓	…	✓	…	…	✓
IC 5332	9.67	−10.05	1	…	…	✓	✓	✓	✓	✓	✓	✓	✓
NGC 0628	10.34	−10.10	1	…	…	✓	✓	✓	✓	✓	✓	✓	✓
NGC 0685	10.06	−10.44	2	✓	✓	…	✓	✓	…	✓	…	…	✓
NGC 1068	10.91	−9.27	2	✓	✓	…	✓	✓	…	✓	…	…	✓
NGC 1087	9.94	−9.83	1	…	…	✓	✓	✓	✓	✓	✓	✓	✓
NGC 1097	10.76	−10.08	2	✓	✓	…	✓	✓	…	✓	…	…	✓
NGC 1300	10.62	−10.55	1	…	…	✓	✓	✓	✓	✓	✓	✓	✓
NGC 1317	10.62	−10.94	2	✓	…	✓	✓	✓	…	✓	…	…	✓
NGC 1365	11.00	−9.76	1	…	…	✓	✓	✓	✓	✓	✓	✓	✓
NGC 1385	9.98	−9.66	1	…	…	✓	✓	✓	✓	✓	✓	✓	✓
NGC 1433	10.87	−10.82	1	…	…	✓	✓	✓	✓	✓	✓	✓	✓
NGC 1511	9.91	−9.55	2	✓	✓	…	✓	✓	…	✓	…	…	✓
NGC 1512	10.72	−10.61	1	…	…	✓	✓	✓	✓	✓	✓	✓	✓
NGC 1546	10.35	−10.43	2	✓	✓	…	✓	✓	…	✓	…	…	✓
NGC 1559	10.36	−9.79	2	✓	✓	…	✓	✓	…	✓	…	…	✓
NGC 1566	10.79	−10.13	1	…	…	✓	✓	✓	✓	✓	✓	✓	✓
NGC 1637	9.95	−10.14	2	✓	✓	…	✓	✓	…	✓	…	…	✓
NGC 1672	10.73	−9.85	1	…	…	✓	✓	✓	✓	✓	✓	✓	✓
NGC 1792	10.61	−10.04	2	✓	✓	…	✓	✓	…	✓	…	…	✓
NGC 1808	10.29	−9.39	2	✓	✓	…	✓	✓	…	✓	…	…	✓
NGC 1809	9.77	−9.01	2	✓	✓	…	✓	✓	…	✓	…	…	✓
NGC 2090	10.04	−10.43	2	✓	✓	…	✓	✓	…	✓	…	…	✓
NGC 2283	9.89	−10.17	2	✓	✓	…	✓	✓	…	✓	…	…	✓
NGC 2566	10.71	−9.77	2	✓	…	✓	✓	✓	…	✓	…	…	✓
NGC 2775	11.07	−11.13	2	✓	✓	…	✓	✓	…	✓	…	…	✓
NGC 2835	10.00	−9.90	1	…	…	✓	✓	✓	✓	✓	✓	✓	✓
NGC 2903	10.63	−10.15	2	✓	✓	…	✓	✓	…	✓	…	…	✓
NGC 2997	10.73	−10.09	2	✓	✓	…	✓	✓	…	✓	…	…	✓
NGC 3059	10.38	−10.00	2	✓	✓	…	✓	✓	…	✓	…	…	✓
NGC 3137	9.88	−10.19	2	✓	✓	…	✓	✓	…	✓	…	…	✓
NGC 3239	9.17	−9.58	2	✓	✓	…	✓	✓	…	✓	…	…	✓
NGC 3344	10.05	−10.14	2	✓	✓	…	✓	✓	…	✓	…	…	✓
NGC 3351	10.37	−10.25	1	…	…	✓	✓	✓	✓	✓	✓	✓	✓
NGC 3368	10.74	−10.88	2	✓	✓	…	✓	✓	…	✓	…	…	✓
NGC 3507	10.40	−10.40	2	✓	✓	…	✓	✓	…	✓	…	…	✓
NGC 3511	10.03	−10.12	2	✓	✓	…	✓	✓	…	✓	…	…	✓
NGC 3521	11.02	−10.45	2	✓	✓	…	✓	✓	…	✓	…	…	✓
NGC 3596	9.66	−10.18	2	✓	✓	…	✓	✓	…	✓	…	…	✓
NGC 3621	10.06	−10.06	2	✓	✓	…	✓	✓	…	✓	…	…	✓
NGC 3626	10.46	−11.13	2	✓	…	✓	✓	✓	…	✓	…	…	✓
NGC 3627	10.84	−10.25	1	…	…	✓	✓	✓	✓	✓	✓	✓	✓
NGC 4254	10.42	−9.93	1	…	…	✓	✓	✓	✓	✓	✓	✓	✓
NGC 4298	10.02	−10.36	2	✓	✓	…	✓	✓	…	✓	…	…	✓
NGC 4303	10.51	−9.78	1	…	…	✓	✓	✓	✓	✓	✓	✓	✓
NGC 4321	10.75	−10.20	1	…	…	✓	✓	✓	✓	✓	✓	✓	✓
NGC 4424	9.91	−10.43	2	✓	✓	…	✓	✓	…	✓	…	…	✓
NGC 4457	10.42	−10.93	2	✓	✓	…	✓	✓	…	✓	…	…	✓
NGC 4496A	9.53	−9.74	2	✓	…	✓	✓	✓	…	✓	…	…	✓
NGC 4535	10.54	−10.20	1	…	…	✓	✓	✓	✓	✓	✓	✓	✓
NGC 4536	10.40	−9.86	2	✓	…	✓	✓	✓	…	✓	…	…	✓
NGC 4540	9.79	−10.56	2	✓	✓	…	✓	✓	…	✓	…	…	✓
NGC 4548	10.69	−10.97	2	✓	✓	…	✓	✓	…	✓	…	…	✓
NGC 4569	10.81	−10.68	2	✓	✓	…	✓	✓	…	✓	…	…	✓
NGC 4571	10.09	−10.63	2	✓	✓	…	✓	✓	…	✓	…	…	✓
NGC 4579	11.15	−10.81	2	✓	…	✓	✓	✓	…	✓	…	…	✓
NGC 4654	10.57	−9.99	2	✓	✓	…	✓	✓	…	✓	…	…	✓
NGC 4689	10.22	−10.61	2	✓	…	✓	✓	✓	…	✓	…	…	✓
NGC 4694	9.86	−10.66	2	✓	✓	…	✓	✓	…	✓	…	…	✓
NGC 4731	9.48	−9.70	2	✓	…	✓	✓	✓	…	✓	…	…	✓
NGC 4781	9.64	−9.96	2	✓	✓	…	✓	✓	…	✓	…	…	✓
NGC 4826	10.24	−10.93	2	✓	✓	…	✓	✓	…	✓	…	…	✓

Table 3
(Continued)

Galaxy	$\log M_*$ ($M_\odot$)	$\log \mathrm{SFR}/M_*$ (yr^{-1})	Cycle	F150W	F187N	F200W	F300M	F335M	F360M	F770W	F1000W	F1130W	F2100W
NGC 4941	10.17	−10.53	2	✓	✓	…	✓	✓	…	✓	…	…	✓
NGC 4951	9.79	−10.24	2	✓	✓	…	✓	✓	…	✓	…	…	✓
NGC 5042	9.90	−10.12	2	✓	✓	…	✓	✓	…	✓	…	…	✓
NGC 5068	9.41	−9.97	1	…	…	✓	✓	✓	✓	✓	✓	✓	✓
NGC 5134	10.41	−10.75	2	✓	…	✓	✓	✓	…	✓	…	…	✓
NGC 5248	10.41	−10.05	2	✓	✓	…	✓	✓	…	✓	…	…	✓
NGC 5643	10.34	−9.92	2	✓	✓	…	✓	✓	…	✓	…	…	✓
NGC 6300	10.47	−10.19	2	✓	✓	…	✓	✓	…	✓	…	…	✓
NGC 7456	9.64	−10.08	2	✓	✓	…	✓	✓	…	✓	…	…	✓
NGC 7496	10.00	−9.65	1	…	…	✓	✓	✓	✓	✓	✓	✓	✓
Total	…	…	…	54	45	28	73	73	19	73	19	19	73

Note. Columns: $\log M_*$—global stellar mass; $\log \mathrm{SFR}/M_*$—global specific SFR; Cycle—JWST observing cycle when the galaxy was observed (Cycle 1 corresponds to program #2107; Cycle 2 corresponds to program #3707). The remaining columns show which JWST bands have observations (✓) for each galaxy. The bottom row shows the total number of galaxies observed in each band.

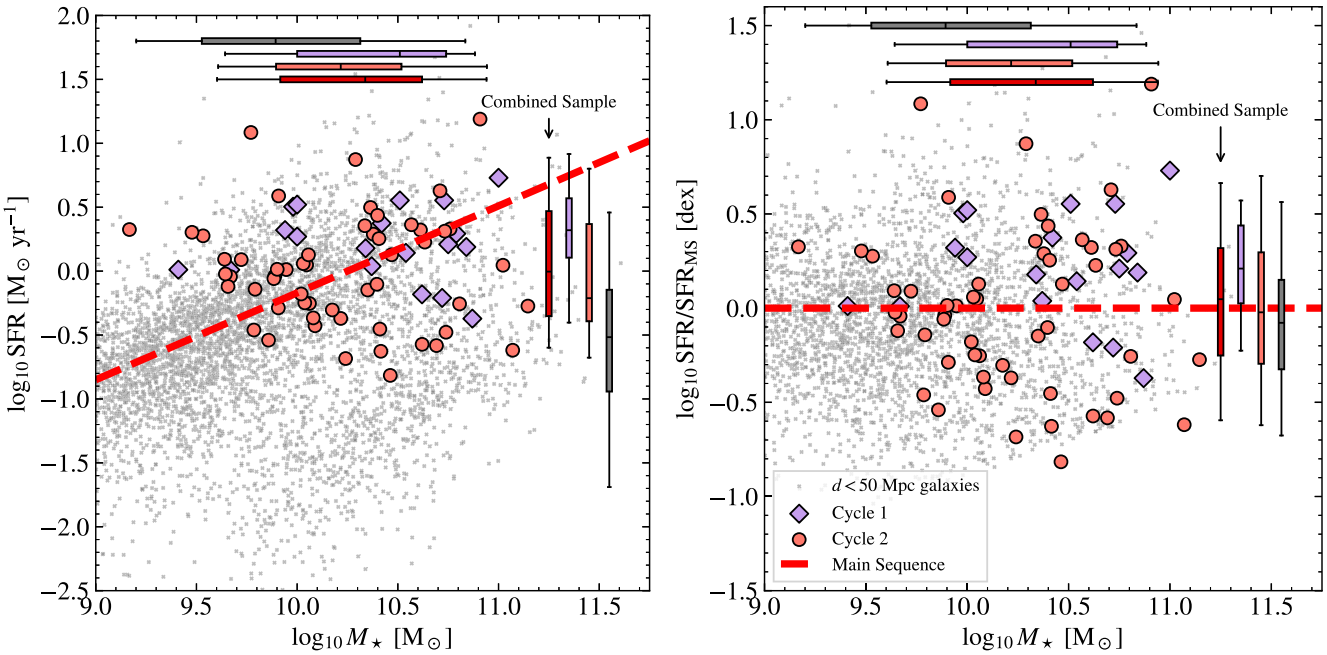

Figure 5. PHANGS-JWST samples relative to the star-forming main sequence. The reference line in the left panel is derived from Equation (19) of A. K. Leroy et al. (2019), with a slope of 0.68 and a y-intercept of $-6.97\ M_\odot\ \mathrm{yr}^{-1}$. The box plots show the median and 16th and 84th percentiles, while the whiskers show the 5th and 95th percentiles. The red box and whiskers show that Cycle 1 + Cycle 2 PHANGS-JWST galaxies cover about 1 dex in stellar mass and approximately ±0.5 dex about the main sequence. The Cycle 1 targets have higher masses and SFRs than the rest of the sample.

new survey targets 55 galaxies, expanding on the 19 in the original sample. Compared to the original sample, these new observations expand to cover galaxies with lower mass and lower specific SFR. Taken together, the two surveys sample the main sequence of star-forming galaxies over the range $\log M_\star/M_\odot \approx 9.75 - 10.75$, i.e., within about 1 dex of the knee in the galaxy mass function and covering the main region of SFR–$M_\star$ parameter space (Figure 5) where stars form at $z = 0$ (see A. K. Leroy et al. 2021). In order to cover this large sample, the current survey focused on two PAH-sensitive filters (F335M and F770W) and did not use the F1130W filter employed by J. C. Lee et al. (2023). The Cycle 2 survey also did not observe the F360M filter that was included by J. C. Lee et al. (2023), and we shifted the short-wavelength starlight-sensitive filter from F200W to F150W in order to avoid wavelength overlap with the F187N filter. We added the F187N filter (which was not observed by J. C. Lee et al. 2023) wherever it captures the Paschen-α line. This yields Paschen-α imaging, which should open a powerful new scientific space (high-resolution imaging of recent star formation).

The observations consisted of MIRI mosaics using the F770W and F2100W filters, with ≈88 s exposure time per point at F770W and ≈344 s at F2100W. The coverage of each mosaic was designed to match the extent of the galaxy in the ≈12 μm emission captured by WISE band 3 (E. L. Wright et al. 2010). Roll angle constraints, row offsets, and other aspects of the observation were designed to meet this goal. As in J. C. Lee et al. (2023) and T. G. Williams et al. (2024), the MIRI

observations were paired in a noninterruptible sequence with single-field off-galaxy observations designed to measure the local background.

In parallel with the background observations, we observed the center of the galaxy with NIRCam module B using the F150W (integration time 215 s), F187N (covering the Paschen-α line, 386 s), F300M (215 s), and F335M (covering the 3.3 μm PAH feature, 386 s) filters. In a few cases where the redshift of the galaxy was too large for the F187N filter to capture the Paschen-α line, we observed using the F200W filter instead. The $2\farcm2 \times 2\farcm2$ NIRCam field covers a large portion of each galaxy ($\approx 6 \times 6$ kpc at 10 Mpc and $\approx 12 \times 12$ kpc at 20 Mpc). The offset between NIRCam and MIRI was enough to allow the MIRI observations to reach a sky position off the galaxy.

As discussed in Section 3, we processed the data using `pjpipe`, the modified version of the STScI pipeline described in J. C. Lee et al. (2023) and T. G. Williams et al. (2024). Refinements to the procedures involved in T. G. Williams et al. (2024) are ongoing. As of this writing, key differences compared to that paper include the following: (1) for MIRI, we have masked out the Lyot coronagraph, as we find this to improve the flux-level match between overlapping tiles; (2) improvements in the "anchoring" (A. K. Leroy et al. 2023b) of the background level to reference data (H. Koziol et al. 2025, in preparation; D. Pathak et al. 2025, in preparation); (3) improved cross-registration between filters (especially relevant to the 3.3 μm and Paschen-α analyses; H. Koziol et al. 2025, in preparation; T. Weinbeck et al. 2025, in preparation); and (4) improved techniques to remove $1/f$-related artifacts from the F187N images (T. Weinbeck et al. 2025, in preparation).

Appendix B
Fits for Individual Galaxies

Table 4 shows the best-fit parameters of the CO(2–1) versus $F335M_{PAH}$, $F770W_{PAH}$, and F1130W relationships for each galaxy. We also report the stellar mass and SFR/$M_\star$ adopted from A. K. Leroy et al. (2019), the brightness of band X in that galaxy at $I_\nu^X = 1$ MJy sr^{-1}, the number of sight lines analyzed, and Spearman's rank correlation coefficient relating the PAH and CO emission for each sight line.

Table 4
Fits to All Pixels Outside Galaxy Centers for Each Galaxy

Name	Cycle	$\log_{10} M_\star$	$\log_{10}$SFR/$M_\star$	m	b	x_0	$\log_{10} C_{band}$	N_{pix}	σ_{pix}	r
				$I_{CO(2-1)}$ versus $F770W_{PAH}$						
IC 1954	2	9.67	−10.11	1.050 ± 0.017	0.199 ± 0.010	0.366	−0.185	16,101	0.09	0.76
IC 5273	2	9.72	−9.99	1.133 ± 0.046	−0.069 ± 0.023	0.226	−0.325	13,117	0.13	0.66
IC 5332	2	9.67	−10.05	0.438 ± 0.010	0.261 ± 0.005	−0.079	0.296	16,281	0.20	0.22
NGC 0628	1	10.34	−10.10	0.689 ± 0.010	0.377 ± 0.008	0.179	0.254	122,222	0.16	0.52
NGC 0685	2	10.06	−10.44	0.986 ± 0.020	−0.083 ± 0.012	−0.027	−0.056	13,882	0.16	0.53
NGC 1087	1	9.94	−9.83	1.046 ± 0.024	0.290 ± 0.021	0.466	−0.198	26,830	0.15	0.73
NGC 1097	2	10.76	−10.08	1.238 ± 0.033	0.307 ± 0.016	0.155	0.115	24,368	0.22	0.57
NGC 1300	1	10.62	−10.55	0.822 ± 0.025	0.189 ± 0.017	0.042	0.155	36,359	0.20	0.47
NGC 1317	2	10.62	−10.94	0.861 ± 0.044	0.816 ± 0.023	0.738	0.181	4659	0.13	0.80
NGC 1365	1	11.00	−9.76	0.983 ± 0.051	0.690 ± 0.053	0.292	0.403	40,810	0.25	0.46
NGC 1385	1	9.98	−9.66	0.885 ± 0.019	0.377 ± 0.015	0.560	−0.118	34,515	0.17	0.72
NGC 1433	1	10.87	−10.82	1.176 ± 0.070	0.119 ± 0.048	−0.069	0.200	19,809	0.24	0.50
NGC 1511	2	9.91	−9.55	0.904 ± 0.018	0.623 ± 0.013	0.811	−0.111	12,884	0.11	0.78
NGC 1512	1	10.72	−10.61	0.833 ± 0.027	0.172 ± 0.014	0.009	0.164	14,121	0.16	0.41
NGC 1546	2	10.35	−10.43	0.916 ± 0.023	0.961 ± 0.013	0.848	0.184	11,723	0.05	0.91
NGC 1559	2	10.36	−9.79	0.943 ± 0.025	0.537 ± 0.017	0.763	−0.182	46,456	0.16	0.70
NGC 1566	1	10.79	−10.13	0.905 ± 0.015	0.366 ± 0.014	0.335	0.063	87,712	0.22	0.68
NGC 1637	2	9.95	−10.14	1.028 ± 0.029	0.124 ± 0.018	0.121	−0.001	39,715	0.15	0.66
NGC 1672	1	10.73	−9.85	1.066 ± 0.030	0.364 ± 0.021	0.371	−0.031	23,689	0.20	0.66
NGC 1792	2	10.61	−10.04	1.097 ± 0.025	0.775 ± 0.015	0.896	−0.209	24,488	0.12	0.84
NGC 1808	2	10.29	−9.39	1.103 ± 0.081	0.983 ± 0.069	0.879	0.014	10,521	0.24	0.78
NGC 1809	2	9.77	−9.01	1.134 ± 0.038	0.085 ± 0.016	0.223	−0.169	7076	0.17	0.53
NGC 2090	2	10.04	−10.43	0.913 ± 0.062	0.493 ± 0.024	0.404	0.124	15,649	0.11	0.63
NGC 2283	2	9.89	−10.17	0.927 ± 0.047	0.080 ± 0.027	0.261	−0.162	26,500	0.19	0.52
NGC 2566	2	10.71	−9.77	0.987 ± 0.018	0.307 ± 0.011	0.230	0.080	35,872	0.24	0.57
NGC 2775	2	11.07	−11.13	0.856 ± 0.023	0.355 ± 0.009	0.138	0.237	44,187	0.13	0.47
NGC 2835	1	10.00	−9.90	0.790 ± 0.021	0.172 ± 0.015	0.149	0.054	36,639	0.20	0.42
NGC 2903	2	10.63	−10.15	0.944 ± 0.026	0.623 ± 0.019	0.674	−0.013	64,047	0.14	0.73
NGC 2997	2	10.73	−10.09	1.050 ± 0.012	0.349 ± 0.008	0.267	0.069	44,985	0.15	0.70
NGC 3059	2	10.38	−10.00	0.939 ± 0.017	0.293 ± 0.018	0.355	−0.040	61,109	0.18	0.64
NGC 3137	2	9.88	−10.19	0.956 ± 0.067	0.354 ± 0.020	0.348	0.021	4956	0.08	0.53
NGC 3239	2	9.17	−9.58	0.573 ± 0.048	0.073 ± 0.016	0.222	−0.055	1640	0.17	0.30
NGC 3351	1	10.37	−10.25	0.650 ± 0.016	0.320 ± 0.008	0.051	0.287	29,148	0.17	0.33
NGC 3507	2	10.40	−10.40	0.907 ± 0.020	0.127 ± 0.011	0.026	0.103	32,339	0.17	0.49
NGC 3511	2	10.03	−10.12	1.185 ± 0.025	0.514 ± 0.011	0.645	−0.250	11,678	0.08	0.76
NGC 3521	2	11.02	−10.45	1.155 ± 0.031	0.869 ± 0.017	1.001	−0.287	69,658	0.10	0.85

Table 4
(Continued)

Name	Cycle	$\log_{10} M_\star$	$\log_{10}\mathrm{SFR}/M_\star$	m	b	x_0	$\log_{10} C_{\mathrm{band}}$	N_{pix}	σ_{pix}	r
NGC 3596	2	9.66	−10.18	0.814 ± 0.019	0.349 ± 0.012	0.236	0.157	36,060	0.17	0.57
NGC 3621	2	10.06	−10.06	1.161 ± 0.021	0.561 ± 0.012	0.761	−0.322	38,133	0.13	0.75
NGC 3626	2	10.46	−11.13	0.814 ± 0.036	0.572 ± 0.014	0.509	0.158	4036	0.14	0.62
NGC 3627	1	10.84	−10.25	0.993 ± 0.013	0.743 ± 0.012	0.736	0.012	67,198	0.18	0.72
NGC 4254	1	10.42	−9.93	1.016 ± 0.019	0.562 ± 0.013	0.570	−0.017	65,123	0.14	0.78
NGC 4298	2	10.02	−10.36	0.967 ± 0.046	0.518 ± 0.021	0.377	0.153	20,937	0.07	0.75
NGC 4303	1	10.51	−9.78	0.844 ± 0.019	0.644 ± 0.013	0.660	0.086	29,397	0.18	0.67
NGC 4321	1	10.75	−10.20	0.935 ± 0.007	0.479 ± 0.005	0.282	0.215	37,681	0.16	0.63
NGC 4424	2	9.91	−10.43	0.816 ± 0.064	0.406 ± 0.048	0.480	0.014	4800	0.23	0.57
NGC 4457	2	10.42	−10.93	0.646 ± 0.051	0.537 ± 0.030	0.124	0.457	14,785	0.21	0.44
NGC 4496A	2	9.53	−9.74	0.759 ± 0.024	0.170 ± 0.014	0.161	0.048	12,392	0.18	0.41
NGC 4535	1	10.54	−10.20	0.971 ± 0.038	0.338 ± 0.029	0.158	0.184	31,294	0.17	0.60
NGC 4536	2	10.40	−9.86	1.110 ± 0.023	0.339 ± 0.020	0.350	−0.049	17,043	0.15	0.74
NGC 4540	2	9.79	−10.56	0.788 ± 0.046	0.392 ± 0.021	0.276	0.174	10,939	0.16	0.48
NGC 4548	2	10.69	−10.97	1.002 ± 0.020	0.210 ± 0.010	0.014	0.196	8294	0.16	0.54
NGC 4569	2	10.81	−10.68	0.841 ± 0.018	0.837 ± 0.011	0.598	0.334	14,984	0.11	0.63
NGC 4571	2	10.09	−10.63	0.548 ± 0.019	0.280 ± 0.009	−0.029	0.296	26,226	0.14	0.28
NGC 4579	2	11.15	−10.81	0.833 ± 0.039	0.356 ± 0.022	0.106	0.268	25,120	0.15	0.54
NGC 4654	2	10.57	−9.99	1.051 ± 0.027	0.474 ± 0.020	0.512	−0.064	27,373	0.13	0.78
NGC 4689	2	10.22	−10.61	0.861 ± 0.021	0.356 ± 0.013	0.133	0.241	45,635	0.14	0.59
NGC 4694	2	9.86	−10.66	0.821 ± 0.059	0.294 ± 0.044	0.360	−0.002	2720	0.21	0.54
NGC 4731	2	9.48	−9.70	0.937 ± 0.028	0.002 ± 0.014	0.279	−0.259	4894	0.18	0.51
NGC 4781	2	9.64	−9.96	1.064 ± 0.013	0.265 ± 0.008	0.491	−0.257	29,714	0.12	0.75
NGC 4826	2	10.24	−10.93	1.015 ± 0.044	1.084 ± 0.027	1.013	0.056	22,873	0.11	0.83
NGC 4941	2	10.17	−10.53	0.795 ± 0.024	0.261 ± 0.006	0.034	0.234	5447	0.07	0.37
NGC 4951	2	9.79	−10.24	1.092 ± 0.039	0.372 ± 0.014	0.480	−0.153	6724	0.16	0.55
NGC 5042	2	9.90	−10.12	0.891 ± 0.018	0.094 ± 0.008	0.109	−0.003	15,685	0.19	0.40
NGC 5068	1	9.41	−9.97	0.690 ± 0.021	0.282 ± 0.016	0.182	0.156	67,372	0.23	0.39
NGC 5134	2	10.41	−10.75	0.737 ± 0.025	0.196 ± 0.013	0.117	0.110	19,250	0.20	0.44
NGC 5248	2	10.41	−10.05	0.962 ± 0.020	0.503 ± 0.014	0.433	0.087	51,724	0.14	0.71
NGC 5643	2	10.34	−9.92	0.853 ± 0.015	0.385 ± 0.010	0.363	0.076	76,446	0.19	0.61
NGC 6300	2	10.47	−10.19	0.905 ± 0.017	0.481 ± 0.012	0.383	0.134	84,152	0.19	0.58
NGC 7456	2	9.64	−10.08	0.638 ± 0.114	0.138 ± 0.016	0.200	0.011	907	0.06	0.26
NGC 7496	1	10.00	−9.65	1.032 ± 0.013	0.062 ± 0.009	0.137	−0.080	15,593	0.15	0.68
				$I_{\mathrm{CO(2-1)}}$ versus $\mathrm{F335M_{PAH}}$						
IC 5332	2	9.67	−10.05	0.339 ± 0.046	0.416 ± 0.013	−0.813	0.691	2242	0.18	0.14
NGC 0628	1	10.34	−10.10	0.630 ± 0.017	0.623 ± 0.012	−0.780	1.115	27,463	0.11	0.42
NGC 1087	1	9.94	−9.83	1.211 ± 0.018	0.401 ± 0.013	−0.545	1.062	19,279	0.12	0.73
NGC 1300	1	10.62	−10.55	0.862 ± 0.041	0.589 ± 0.016	−0.703	1.196	5452	0.12	0.50
NGC 1365	1	11.00	−9.76	1.295 ± 0.114	0.842 ± 0.080	−0.526	1.524	5781	0.33	0.37
NGC 1385	1	9.98	−9.66	0.924 ± 0.015	0.632 ± 0.010	−0.387	0.989	19,238	0.11	0.72
NGC 1433	1	10.87	−10.82	1.604 ± 0.280	0.776 ± 0.062	−0.746	1.972	2224	0.32	0.37
NGC 1512	1	10.72	−10.61	0.714 ± 0.061	0.538 ± 0.015	−0.734	1.063	1468	0.08	0.40
NGC 1566	1	10.79	−10.13	0.793 ± 0.013	0.770 ± 0.009	−0.569	1.221	28,985	0.21	0.52
NGC 1672	1	10.73	−9.85	1.126 ± 0.055	0.657 ± 0.028	−0.576	1.305	8502	0.20	0.52
NGC 2835	1	10.00	−9.90	0.803 ± 0.041	0.483 ± 0.018	−0.663	1.015	6072	0.15	0.42
NGC 3351	1	10.37	−10.25	0.722 ± 0.109	0.615 ± 0.025	−0.726	1.139	963	0.23	0.21
NGC 3627	1	10.84	−10.25	1.087 ± 0.022	0.785 ± 0.018	−0.428	1.250	54,452	0.19	0.64
NGC 4254	1	10.42	−9.93	0.905 ± 0.011	0.893 ± 0.006	−0.500	1.345	32,222	0.10	0.66
NGC 4303	1	10.51	−9.78	0.592 ± 0.012	0.999 ± 0.007	−0.466	1.275	9011	0.10	0.54
NGC 4321	1	10.75	−10.20	0.887 ± 0.017	0.818 ± 0.009	−0.667	1.409	8440	0.10	0.59
NGC 4535	1	10.54	−10.20	0.841 ± 0.025	0.847 ± 0.010	−0.611	1.362	4411	0.13	0.50
NGC 5068	1	9.41	−9.97	0.704 ± 0.030	0.460 ± 0.017	−0.679	0.938	26,386	0.21	0.36
NGC 7496	1	10.00	−9.65	0.930 ± 0.048	0.490 ± 0.021	−0.695	1.136	3755	0.13	0.54
				$I_{\mathrm{CO(2-1)}}$ versus F1130W						
IC 5332	2	9.67	−10.05	0.495 ± 0.022	0.251 ± 0.012	0.107	0.199	16,263	0.20	0.23
NGC 0628	1	10.34	−10.10	0.538 ± 0.054	0.513 ± 0.044	0.390	0.304	122,196	0.20	0.53
NGC 1087	1	9.94	−9.83	1.034 ± 0.038	0.312 ± 0.032	0.637	−0.347	26,790	0.16	0.73
NGC 1300	1	10.62	−10.55	0.617 ± 0.078	0.339 ± 0.058	0.228	0.199	36,319	0.23	0.51
NGC 1365	1	11.00	−9.76	1.008 ± 0.060	0.795 ± 0.051	0.551	0.240	40,793	0.24	0.50
NGC 1385	1	9.98	−9.66	0.705 ± 0.055	0.512 ± 0.050	0.725	0.000	34,494	0.21	0.72
NGC 1433	1	10.87	−10.82	1.060 ± 0.059	0.256 ± 0.038	0.200	0.043	19,802	0.22	0.57

Table 4
(Continued)

Name	Cycle	$\log_{10} M_\star$	$\log_{10}\mathrm{SFR}/M_\star$	m	b	x_0	$\log_{10} C_{\mathrm{band}}$	N_{pix}	σ_{pix}	r
NGC 1512	1	10.72	−10.61	0.874 ± 0.021	0.198 ± 0.009	0.219	0.006	14,107	0.16	0.41
NGC 1566	1	10.79	−10.13	0.939 ± 0.026	0.402 ± 0.022	0.562	−0.126	87,693	0.22	0.69
NGC 1672	1	10.73	−9.85	1.070 ± 0.040	0.419 ± 0.027	0.586	−0.209	23,678	0.20	0.67
NGC 2835	1	10.00	−9.90	0.601 ± 0.093	0.333 ± 0.066	0.351	0.121	36,589	0.24	0.43
NGC 3351	1	10.37	−10.25	0.553 ± 0.076	0.325 ± 0.038	0.276	0.172	29,151	0.18	0.29
NGC 3627	1	10.84	−10.25	1.064 ± 0.024	0.780 ± 0.020	0.949	−0.229	67,195	0.19	0.71
NGC 4254	1	10.42	−9.93	1.006 ± 0.039	0.601 ± 0.026	0.741	−0.144	65,123	0.15	0.78
NGC 4303	1	10.51	−9.78	0.952 ± 0.024	0.666 ± 0.016	0.879	−0.170	29,408	0.17	0.69
NGC 4321	1	10.75	−10.20	1.021 ± 0.024	0.517 ± 0.015	0.518	−0.012	37,677	0.16	0.64
NGC 4535	1	10.54	−10.20	1.129 ± 0.058	0.350 ± 0.044	0.345	−0.040	31,296	0.17	0.61
NGC 4826	2	10.24	−10.93	1.198 ± 0.069	1.082 ± 0.038	1.254	−0.421	22,847	0.12	0.81
NGC 5068	1	9.41	−9.97	0.647 ± 0.020	0.313 ± 0.015	0.382	0.066	67,347	0.24	0.40
NGC 7496	1	10.00	−9.65	1.152 ± 0.010	0.069 ± 0.006	0.347	−0.331	15,593	0.14	0.70

Note. Columns: Cycle—Indicates whether the galaxy was observed as part of Cycle 1 (GO 2107) or Cycle 2 (GO 3707); $\log_{10} M_\star$—global stellar mass ($M_\odot$); $\log_{10}\mathrm{SFR}/M_\star$—global specific SFR ($\mathrm{yr}^{-1}$); m, b, x_0—best-fit power-law scaling parameters following Equation (2) relating CO(2–1) to intensity in band X; C_{band}—the normalization of the best-fit relation at $I_\nu^X = 1$ MJy sr^{-1} (K km s^{-1} (MJy sr^{-1})$^{-1}$); N_{pix}—number of sight lines entering the analysis, where approximately four sight lines correspond to one independent measurement; σ_{pix}—rms scatter in $\log_{10}$CO(2–1) intensity about the fit for all sight lines included in bins; r—rank correlation between $\log_{10}$CO(2–1) and intensity in band X for all sight lines.

Appendix C
How to Estimate CO(2–1) Intensity from PAH Emission Maps

We suggest the following recipe, along with some key caveats, to estimate CO(2–1) intensity in units of K km s^{-1} from JWST observations of PAH-dominated filters in units of MJy sr^{-1}.

1. In the case of F335M or F770W, estimate and subtract the associate stellar continuum to calculate $I^{\mathrm{PAH}}_{\mathrm{F335M}}$ or $I^{\mathrm{PAH}}_{\mathrm{F770W}}$. Specifically, subtract $0.22 \times I_{\mathrm{F300M}}$ or $0.13 \times I_{\mathrm{F200W}}$ from I_{F770W} (see Section 3.1 and J. Sutter et al. 2024). If this is not possible, we view F335M as not useful, while F770W can be used with our provided equations but will be biased high in regions of high stellar-to-dust ratios, including stellar bars and bulges. We do not consider stellar continuum correction necessary for F1130W.
2. For a disk galaxy with inclination i, correct the surface brightness by multiplying by $\cos i$.
3. If the specific SFR, $\mathrm{SFR}/M_\star$, is known (e.g., from A. K. Leroy et al. 2019) and the galaxy resembles a low-redshift star-forming galaxy (so that our corrections could be expected to apply), evaluate Equation (3) to obtain $C^{\mathrm{F770W}}_{\mathrm{norm}}$. The best-fit parameters of Equation (3) for all the bands are shown in Table 5. We prefer the $\mathrm{SFR}/M_\star$-based correction. For F335M$_{\mathrm{PAH}}$ and F1130W, we recommend multiplying $C^{\mathrm{PAH}}_{\mathrm{F770W}}$ (top right panel of Figure 2) by typical band ratios $\mathrm{F335M_{PAH}}/\mathrm{F770W_{PAH}} \approx 0.04$ or $\mathrm{F1130W}/\mathrm{F770W_{PAH}} \approx 0.69$ (using x_0 from Table 2) to yield $C^{\mathrm{PAH}}_{\mathrm{F335M}}$ and C_{F1130W}, respectively. If this step is not possible, one can make a less accurate estimate by applying the general relation (i.e., simply use the appropriate equation from Table 2 and ignore the following step). In this case, one should expect ≈0.2 dex bias in the predicted CO(2–1) map for any individual galaxy.
4. If $\log_{10} C_{\mathrm{norm}}$ has been estimated, subtract this from the observed $\log_{10} I^{\mathrm{PAH}}_{\mathrm{F770W}}$ for each sight line to remove the galaxy-to-galaxy normalization. Then, for F770W$_{\mathrm{PAH}}$, plug this normalized intensity, x, into Equation (5) to estimate $y \equiv \log_{10} I_{\mathrm{CO(2-1)}}$. For F335M$_{\mathrm{PAH}}$,

$$y = (0.93 \pm 0.09)(x - 0.10) + (0.13 \pm 0.06), \quad \text{(C1)}$$

where x and y are defined as in Equation (5) and the full Cycle 1 data set shows 0.42 dex rms scatter in the residuals. Similarly, for F1130W, we find

$$y = (1.01 \pm 0.09)(x - 1.34) + (1.27 \pm 0.08). \quad \text{(C2)}$$

The best-fit parameters to Equation (5) for all PAH bands are shown in Table 6.

This procedure will predict the CO(2–1) intensity. In many cases, the molecular gas mass will be the quantity of direct interest. In future work, we aim to explore how $I^{\mathrm{PAH}}_{\mathrm{F770W}}$ compares to N(H) directly. For now, to convert from CO intensity to molecular gas column or surface density, one should multiply the predicted CO maps by an appropriate CO(2–1)-to-H_2 conversion factor. A. D. Bolatto et al. (2013) review the CO-to-H_2 conversion factor, and E. Schinnerer & A. K. Leroy (2024) provide current prescriptions that attempt to account for variations in opacity, CO excitation, and metallicity.

Table 5
Best-fit Parameters for $\log_{10} C$ vs. Global Galaxy Properties

Band	N_{gal}	m	b	x_0	r	σ_{line}	σ_{data}
Fits versus $\log_{10}$ SFR$/M_\star$ (yr^{-1})							
F335M$_{PAH}$	19	-0.32 ± 0.18	1.20 ± 0.06	-10.05	-0.38	0.22	0.20
F770W$_{PAH}$	70	-0.21 ± 0.04	0.03 ± 0.02	-10.14	-0.50	0.13	0.17
F770W	70	-0.17 ± 0.04	-0.00 ± 0.02	-10.14	-0.42	0.12	0.17
F1130W	20	-0.01 ± 0.13	-0.03 ± 0.05	-10.08	-0.01	0.25	0.25
Fits versus $\log_{10} M_\star$ ($M_\odot$)							
F335M$_{PAH}$	19	0.44 ± 0.10	1.26 ± 0.04	10.51	0.74	0.14	0.20
F770W$_{PAH}$	70	0.15 ± 0.04	0.06 ± 0.02	10.34	0.38	0.16	0.17
F770W	70	0.12 ± 0.04	0.02 ± 0.02	10.34	0.32	0.17	0.17
F1130W	20	0.01 ± 0.11	-0.03 ± 0.05	10.47	0.02	0.25	0.25

Note. Fit results for CO(2–1) normalization versus galaxy properties. m is the slope, b is the intercept, x_0 is the pivot point, r is the Pearson correlation coefficient, σ_{line} is the scatter about the fit, and σ_{data} is the scatter in the y-direction. The top row of Figure 1 shows the fits for F770W$_{PAH}$.

Table 6
Ratios, Correlation, and Scaling Relations between PAH and CO(2–1) Emission

X	N_{gal}	N^a_{pix}	$\log_{10}$CO$/X$	r	b	m	x_0	σ
All Pixels								
F335M$_{PAH}$	19	296,834	0.08 ± 0.36	0.57	0.13 ± 0.06	0.93 ± 0.09	0.10	0.42
F770W$_{PAH}$	70	2,090,731	-0.02 ± 0.32	0.68	1.36 ± 0.06	0.88 ± 0.06	1.44	0.43
F770W	70	2,120,025	-0.02 ± 0.33	0.68	1.41 ± 0.07	0.90 ± 0.06	1.47	0.43
F1130W	20	972,892	-0.12 ± 0.38	0.67	1.27 ± 0.08	1.01 ± 0.09	1.34	0.46
All Pixels Outside of Centers								
F335M$_{PAH}$	19	279,910	0.06 ± 0.36	0.55	-0.04 ± 0.07	1.00 ± 0.11	-0.05	0.42
F770W$_{PAH}$	70	2,041,245	-0.02 ± 0.32	0.67	1.12 ± 0.07	0.98 ± 0.08	1.16	0.41
F770W	70	2,069,574	-0.02 ± 0.33	0.67	1.16 ± 0.08	1.02 ± 0.09	1.19	0.41
F1130W	20	946,437	-0.12 ± 0.38	0.66	1.03 ± 0.09	1.14 ± 0.14	1.11	0.45
All Pixels in Centers								
F335M$_{PAH}$	17	16,915	0.32 ± 0.39	0.71	0.35 ± 0.07	0.71 ± 0.09	0.10	0.42
F770W$_{PAH}$	58	49,469	0.00 ± 0.33	0.88	1.38 ± 0.07	0.87 ± 0.07	1.44	0.41
F770W	58	50,434	-0.02 ± 0.33	0.88	1.40 ± 0.07	0.91 ± 0.07	1.47	0.43
F1130W	18	26,443	-0.21 ± 0.37	0.91	1.15 ± 0.07	1.15 ± 0.09	1.34	0.40
All Pixels in Nebular Regions (Cycle 1 Only)								
F335M$_{PAH}$	19	119,051	0.02 ± 0.32	0.66	-0.05 ± 0.07	1.03 ± 0.12	-0.05	0.38
F770W$_{PAH}$	19	186,605	-0.12 ± 0.32	0.79	0.95 ± 0.09	1.07 ± 0.10	1.09	0.39
F770W	19	187,137	-0.11 ± 0.31	0.79	1.00 ± 0.08	1.11 ± 0.10	1.12	0.39
F1130W	19	194,681	-0.18 ± 0.35	0.79	0.93 ± 0.09	1.20 ± 0.14	1.11	0.41
All Pixels in Diffuse Regions (Cycle 1 Only)								
F335M$_{PAH}$	19	160,845	0.10 ± 0.38	0.44	-0.26 ± 0.10	1.24 ± 0.30	-0.40	0.44
F770W$_{PAH}$	19	632,119	-0.02 ± 0.35	0.58	0.66 ± 0.12	1.30 ± 0.28	0.66	0.45
F770W	19	642,906	-0.02 ± 0.35	0.57	0.70 ± 0.12	1.35 ± 0.26	0.70	0.45
F1130W	19	727,342	-0.11 ± 0.38	0.58	0.75 ± 0.12	1.40 ± 0.23	0.81	0.46

Note. Fit results for CO(2–1) normalization versus galaxy properties. m is the slope, b is the intercept, x_0 is the pivot point, r is the Pearson correlation coefficient, and σ is the scatter about the fit. Each section of the table reports results for a different data selection. Before fitting, the CO intensities for each galaxy were scaled by the predicted normalization based on the fit of normalization versus $\log_{10}$SFR$/M_\star$ (Figure 2, Table 5).

ORCID iDs

Ryan Chown https://orcid.org/0000-0001-8241-7704
Adam K. Leroy https://orcid.org/0000-0002-2545-1700
Karin Sandstrom https://orcid.org/0000-0002-4378-8534
Jérémy Chastenet https://orcid.org/0000-0002-5235-5589
Jessica Sutter https://orcid.org/0000-0002-9183-8102
Eric W. Koch https://orcid.org/0000-0001-9605-780X
Hannah B. Koziol https://orcid.org/0009-0001-5949-1524
Lukas Neumann https://orcid.org/0000-0001-9793-6400
Jiayi Sun https://orcid.org/0000-0003-0378-4667
Thomas G. Williams https://orcid.org/0000-0002-0012-2142
Dalya Baron https://orcid.org/0000-0003-4974-3481
Gagandeep S. Anand https://orcid.org/0000-0002-5259-2314
Ashley. T. Barnes https://orcid.org/0000-0003-0410-4504
Zein Bazzi https://orcid.org/0009-0001-1221-0975
Francesco Belfiore https://orcid.org/0000-0002-2545-5752
Frank Bigiel https://orcid.org/0000-0003-0166-9745
Alberto Bolatto https://orcid.org/0000-0002-5480-5686
Médéric Boquien https://orcid.org/0000-0003-0946-6176
Yixian Cao https://orcid.org/0000-0001-5301-1326
Mélanie Chevance https://orcid.org/0000-0002-5635-5180
Dario Colombo https://orcid.org/0000-0001-6498-2945
Daniel A. Dale https://orcid.org/0000-0002-5782-9093
Jakob den Brok https://orcid.org/0000-0002-8760-6157
Oleg V. Egorov https://orcid.org/0000-0002-4755-118X
Cosima Eibensteiner https://orcid.org/0000-0002-1185-2810
Eric Emsellem https://orcid.org/0000-0002-6155-7166
Hamid Hassani https://orcid.org/0000-0002-8806-6308
Jonathan D. Henshaw https://orcid.org/0000-0001-9656-7682
Hao He https://orcid.org/0000-0001-9020-1858
Jaeyeon Kim https://orcid.org/0000-0002-0432-6847
Ralf S. Klessen https://orcid.org/0000-0002-0560-3172
Kathryn Kreckel https://orcid.org/0000-0001-6551-3091
Kirsten L. Larson https://orcid.org/0000-0003-3917-6460
Janice C. Lee https://orcid.org/0000-0002-2278-9407
Sharon E. Meidt https://orcid.org/0000-0002-6118-4048
Eric J. Murphy https://orcid.org/0000-0001-7089-7325
Elias K. Oakes https://orcid.org/0000-0002-0119-1115
Eve C. Ostriker https://orcid.org/0000-0002-0509-9113
Hsi-An Pan https://orcid.org/0000-0002-1370-6964
Debosmita Pathak https://orcid.org/0000-0003-2721-487X
Erik Rosolowsky https://orcid.org/0000-0002-5204-2259
Sumit K. Sarbadhicary https://orcid.org/0000-0002-4781-7291
Eva Schinnerer https://orcid.org/0000-0002-3933-7677
Yu-Hsuan Teng https://orcid.org/0000-0003-4209-1599
David A. Thilker https://orcid.org/0000-0002-8528-7340
Tony D. Weinbeck https://orcid.org/0009-0005-8923-558X
Elizabeth J. Watkins https://orcid.org/0000-0002-7365-5791

References

Allamandola, L. J., Tielens, A. G. G. M., & Barker, J. R. 1989, ApJS, 71, 733
Aniano, G., Draine, B. T., Gordon, K. D., & Sandstrom, K. 2011, PASP, 123, 1218
Aniano, G., Draine, B. T., Hunt, L. K., et al. 2020, ApJ, 889, 150
Astropy Collaboration, Price-Whelan, A. M., Lim, P. L., et al. 2022, ApJ, 935, 167
Astropy Collaboration, Price-Whelan, A. M., Sipőcz, B. M., et al. 2018, AJ, 156, 123
Astropy Collaboration, Robitaille, T. P., Tollerud, E. J., et al. 2013, A&A, 558, A33
Barnes, A. T., Chandar, R., Kreckel, K., et al. 2022, A&A, 662, L6
Baron, D., Netzer, H., Lutz, D., Davies, R. I., & Prochaska, J. X. 2024a, ApJ, 968, 23
Baron, D., Sandstrom, K. M., Rosolowsky, E., et al. 2024b, ApJ, 968, 24
Belfiore, F., Leroy, A. K., Williams, T. G., et al. 2023, A&A, 678, A129
Bolatto, A. D., Levy, R. C., Tarantino, E., et al. 2024, ApJ, 967, 63
Bolatto, A. D., Wolfire, M., & Leroy, A. K. 2013, ARA&A, 51, 207
Boulanger, F., & Perault, M. 1988, ApJ, 330, 964
Calzetti, D., Kennicutt, R. C., Engelbracht, C. W., et al. 2007, ApJ, 666, 870
Chastenet, J., Sandstrom, K. M., Leroy, A. K., et al. 2025, ApJS, 273, 13
Chastenet, J., Sutter, J., Sandstrom, K., et al. 2023a, ApJL, 944, L12
Chastenet, J., Sutter, J., Sandstrom, K., et al. 2023b, ApJL, 944, L11
Chiang, I.-D., Sandstrom, K. M., Chastenet, J., et al. 2024, ApJ, 964, 18
Chown, R., Li, C., Parker, L., et al. 2021, MNRAS, 500, 1261
Chown, R., Sidhu, A., Peeters, E., et al. 2024, A&A, 685, A75
Compiègne, M., Abergel, A., Verstraete, L., & Habart, E. 2008, A&A, 491, 797
Compiègne, M., Flagey, N., Noriega-Crespo, A., et al. 2010, ApJL, 724, L44
Dale, D. A., Graham, G. B., Barnes, A. T., et al. 2025, AJ, 169, 133
Doré, O., Werner, M. W., Ashby, M. L. N., et al. 2018, arXiv:1805.05489
Draine, B. T. 2011, Physics of the Interstellar and Intergalactic Medium (Princeton, NJ: Princeton Univ. Press)
Draine, B. T., Dale, D. A., Bendo, G., et al. 2007, ApJ, 663, 866
Draine, B. T., & Li, A. 2007, ApJ, 657, 810
Draine, B. T., Li, A., Hensley, B. S., et al. 2021, ApJ, 917, 3
Egorov, O. V., Kreckel, K., Sandstrom, K. M., et al. 2023, ApJL, 944, L16
Eibensteiner, C., Sun, J., Bigiel, F., et al. 2024, A&A, 691, A163
Emsellem, E., Schinnerer, E., Santoro, F., et al. 2022, A&A, 659, A191
Galliano, F., Galametz, M., & Jones, A. P. 2018, ARA&A, 56, 673
Gao, Y., Tan, Q.-H., Gao, Y., et al. 2022, ApJ, 940, 133
Gao, Y., Xiao, T., Li, C., et al. 2019, ApJ, 887, 172
Gordon, K. D., Engelbracht, C. W., Rieke, G. H., et al. 2008, ApJ, 682, 336
Groves, B., Kreckel, K., Santoro, F., et al. 2023, MNRAS, 520, 4902
Hassani, H., Rosolowsky, E., Leroy, A. K., et al. 2023, ApJL, 944, L21
Hensley, B. S., Murray, C. E., & Dodici, M. 2022, ApJ, 929, 23
Hildebrand, R. H. 1983, QJRAS, 24, 267
Israel, F. P. 1997, A&A, 328, 471
Israel, F. P. 2020, A&A, 635, A131
Kelly, B. C. 2007, ApJ, 665, 1489
Kennicutt, R. C., & Evans, N. J. 2012, ARA&A, 50, 531
Lang, P., Meidt, S. E., Rosolowsky, E., et al. 2020, ApJ, 897, 122
Lebouteiller, V., Brandl, B., Bernard-Salas, J., Devost, D., & Houck, J. R. 2007, ApJ, 665, 390
Lee, J. C., Sandstrom, K. M., Leroy, A. K., et al. 2023, ApJL, 944, L17
Lee, J. C., Whitmore, B. C., Thilker, D. A., et al. 2022, ApJS, 258, 10
Leger, A., & Puget, J. L. 1984, A&A, 137, L5
Leroy, A. K., Bolatto, A., Gordon, K., et al. 2011, ApJ, 737, 12
Leroy, A. K., Bolatto, A. D., Sandstrom, K., et al. 2023a, ApJL, 944, L10
Leroy, A. K., Sandstrom, K. M., Lang, D., et al. 2019, ApJS, 244, 24
Leroy, A. K., Sandstrom, K., Rosolowsky, E., et al. 2023b, ApJL, 944, L9
Leroy, A. K., Schinnerer, E., Hughes, A., et al. 2021, ApJS, 257, 43
Li, J., Kreckel, K., Sarbadhicary, S., et al. 2024, A&A, 690, 161
Linzer, N. B., Kim, J.-G., Kim, C.-G., & Ostriker, E. C. 2024, ApJ, 975, 173
Madden, S. C., Galliano, F., Jones, A. P., & Sauvage, M. 2006, A&A, 446, 877
Maragkoudakis, A., Peeters, E., & Ricca, A. 2020, MNRAS, 494, 642
Meidt, S. E., Rosolowsky, E., Sun, J., et al. 2023, ApJL, 944, L18
Montillaud, J., Joblin, C., & Toublanc, D. 2013, A&A, 552, A15
Neumann, L., den Brok, J. S., Bigiel, F., et al. 2023, A&A, 675, A104
Pathak, D., Leroy, A. K., Thompson, T. A., et al. 2024, AJ, 167, 39
Pedrini, A., Adamo, A., Calzetti, D., et al. 2024, ApJ, 971, 32
Peeters, E., Habart, E., Berné, O., et al. 2024, A&A, 685, A74
Peeters, E., Spoon, H. W. W., & Tielens, A. G. G. M. 2004, ApJ, 613, 986
Pety, J., Teyssier, D., Fossé, D., et al. 2005, A&A, 435, 885
Povich, M. S., Stone, J. M., Churchwell, E., et al. 2007, ApJ, 660, 346
Puget, J. L., & Leger, A. 1989, ARA&A, 27, 161
Querejeta, M., Schinnerer, E., Meidt, S., et al. 2021, A&A, 656, A133
Regan, M. W., Thornley, M. D., Bendo, G. J., et al. 2004, ApJS, 154, 204
Saintonge, A., & Catinella, B. 2022, ARA&A, 60, 319
Saintonge, A., Catinella, B., Tacconi, L. J., et al. 2017, ApJS, 233, 22
Sandstrom, K. M., Chastenet, J., Sutter, J., et al. 2023a, ApJL, 944, L7
Sandstrom, K. M., Koch, E. W., Leroy, A. K., et al. 2023b, ApJL, 944, L8
Sandstrom, K. M., Leroy, A. K., Walter, F., et al. 2013, ApJ, 777, 5
Santoro, F., Kreckel, K., Belfiore, F., et al. 2022, A&A, 658, A188
Schinnerer, E., Emsellem, E., Henshaw, J. D., et al. 2023, ApJL, 944, L15
Schinnerer, E., & Leroy, A. K. 2024, ARA&A, 62, 369
Schruba, A., Leroy, A. K., Walter, F., et al. 2011, AJ, 142, 37
Smith, J. D. T., Draine, B. T., Dale, D. A., et al. 2007, ApJ, 656, 770

Sun, J., Leroy, A. K., Ostriker, E. C., et al. 2020, ApJ, 892, 148
Sutter, J., Sandstrom, K., Chastenet, J., et al. 2024, ApJ, 971, 178
Teng, Y.-H., Sandstrom, K. M., Sun, J., et al. 2023, ApJ, 950, 119
Thilker, D. A., Lee, J. C., Deger, S., et al. 2023, ApJL, 944, L13
Tielens, A. G. G. M. 2008, ARA&A, 46, 289
Whitcomb, C. M., Sandstrom, K., Leroy, A., & Smith, J.-D. T. 2023a, ApJ, 948, 88
Whitcomb, C. M., Sandstrom, K., & Smith, J.-D. T. 2023b, RNAAS, 7, 38
Williams, T., Egorov, O., Rosolowsky, E., et al. 2023, Physics at High Angular Resolution in Nearby GalaxieS—JWST ("PHANGS-JWST"), STScI/MAST, doi:10.17909/ew88-jt15
Williams, T. G., Lee, J. C., Larson, K. L., et al. 2024, ApJS, 273, 13
Wright, E. L., Eisenhardt, P. R. M., Mainzer, A. K., et al. 2010, AJ, 140, 1868